

2006

Buckling of a fibrillar interface

Ajita Rajan
Lehigh University

Follow this and additional works at: <http://preserve.lehigh.edu/etd>

Recommended Citation

Rajan, Ajita, "Buckling of a fibrillar interface" (2006). *Theses and Dissertations*. Paper 919.

This Thesis is brought to you for free and open access by Lehigh Preserve. It has been accepted for inclusion in Theses and Dissertations by an authorized administrator of Lehigh Preserve. For more information, please contact preserve@lehigh.edu.

Rajan, Ajita

**Buckling of a
Fibrillar Interface**

January 2006

BUCKLING OF A FIBRILLAR INTERFACE

by

Ajita Rajan

Presented to the Graduate and Research Committee of Lehigh University in
Candidacy for the Master of Science Degree

in

Chemical Engineering

Lehigh University

December 16, 2005

This thesis is accepted and approved in partial fulfillment of the requirements for the Master of Science.

Date: December 16, 2005

Thesis Advisor
Anand Jagota
Professor of Chemical and
Director, Bioengineering and Life Sciences Program

Associate Chair of the Department
Kemal Tuzla

ACKNOWLEDGEMENTS

It's a pleasure to thank all those who helped contribute towards this thesis.

I am tremendously grateful to Dr. Anand Jagota for his enthusiastic supervision, insightful discussions and patience during this project. I thank Nicholas Glassmaker and my lab mates for all the technical discussions relevant to the project and help with the experimental setup.

I would like to acknowledge the advice, training as well as the hospitality offered by the staff at the Cornell NanoScale Science and Technology Facility at Cornell University. The Microscopy Center at Lehigh University has also offered a great deal of guidance and information to help obtain images of various samples used during this project.

For financial support during my course, I extend my gratitude towards the Women's Center at Lehigh University. I am also thankful to them for their patience and understanding during the busy times.

I am forever grateful to my family for their endless support, advice and encouragement throughout my project and my time at the University. Finally, I thank my friends around campus who have been my surrogate family during my stay here and offered a great deal of moral support, care and attention.

TABLE OF CONTENTS

Abstract	1
<i>Chapter 1</i>	
Introduction	2
<i>Chapter 2</i>	
Design	9
2.1 Design Calculations	10
2.2 Structure specifications	13
<i>Chapter 3</i>	
Processing	14
3.1 Photomask Processing	16
3.2 Making the Silicon Master using Photolithography	17
3.3 Treating the Silicon Master and Glass slides	21
<i>Chapter 4</i>	
Fabrication of PDMS Fibrils	23
<i>Chapter 5</i>	
Scanning Electron Microscope views	25
5.1 SEM views of Silicon Master	26
5.2 SEM views of Fibrillar Sample	27
5.3 Sample structures tested	28

<i>Chapter 6</i>		
Experimental Setup		31
<i>Chapter 7</i>		
Modulus Measurement		35
7.1	Experimental Setup	35
7.2	Calculations and plots	37
<i>Chapter 8</i>		
Experimental Observations and Measurements		40
8.1	Structure 1: 18 micron side x 53 micron height (small spacing)	
8.1.1	Raw data and Stress-Displacement plots	41
8.1.2	Optical Micrographs	42
8.1.3	Observations	43
8.2	Structure 2: 18 micron side x 53 micron height (medium spacing)	
8.2.1	Raw data and Stress-Displacement plots	46
8.2.2	Optical Micrographs	48
8.2.3	Observations	49
8.3	Structure 4: 16 micron side x 53 micron height (small spacing)	
8.3.1	Raw data and Stress-Displacement plots	51
8.3.2	Optical Micrographs	52
8.3.3	Observations	53
8.4	Structure 5: 16 micron side x 53 micron height (medium spacing)	
8.4.1	Raw data and Stress-Displacement plots	55
8.4.2	Optical Micrographs	56
8.4.3	Observations	57

8.5	Structure 6: 16 micron side x 53 micron height (large spacing)	
8.5.1	Raw data and Stress-Displacement plots	59
8.5.2	Optical Micrographs	60
8.5.3	Observations	61
<i>Chapter 9</i>		
	Buckling Theory	63
9.1	Discussion	63
9.2	Plots of Buckling theory and Experimental Values	66
9.3	Observations	67
<i>Chapter 10</i>		
	Conclusions	68
	References	70

LIST OF TABLES

2.1: Specifications for fibrillar structures of varying size and spacing	13
5.1: Structures with fibril cross-section dimensions and spacing as designed	28
5.2: Structures with fibril dimensions and spacing as measured	28
9.1: The equations of lines on the graph of stress (in Pa) vs. the dimensionless parameter $\pi^2 EI/L^2$ representing the classical boundary conditions for buckling struts	65

LIST OF FIGURES

1.1	Lamellar structure of a Tree Dtella, <i>Gehyra variegata</i>	3
1.2 a)	Hierarchical fibrillar structures in <i>G.Gecko</i> , terminating in thin spatulae	4
1.2 b)	Near-tip structure in <i>O. marmorata</i>	4
1.2 c)	Fibrillar and spatular structure in insects	4
1.3	Fibrillar microstructure fabricated by molding polydimethylsiloxane (PDMS), on a Silicon master fabricated using photolithography	7
2.1	Dimensions of the microfibrillar mat	9
2.2	Idealized depictions of undesirable deformation modes for fibrillar structures	10
3.1	Patterning Silicon masters using Photolithography	15
3.2	Schematics of relief pattern on 4" Si master for molding fibrillar structure with varied sizes and densities	20
5.1	Surface of Silicon master with square trenches	26
5.2	Length-wise section of trenches in the Silicon master	26

5.3	Single fibril – Top view	27
5.4	Top view of sample	27
5.5	Sample tilted at 60 degrees	27
5.6	Structures with fibrils having cross-section dimensions of 18x18 microns and 53 microns in height	29
5.7	Structures with fibrils having cross-section dimensions of 16x16 microns and 53 microns in height	30
6.1	Schematic representation of experimental setup for indentation experiments	32
6.2 a)	Raw data representing force vs. time graph for the	34
6.2 b)	Stress vs. displacement graph for the sample	34
6.2 c)	Sample with tips of the fibrils in contact with the glass slide	34
6.2 d)	Sample with fibrils in buckled state	34
7.1	Schematic representation of experimental setup for modulus measurement	36
7.2	Load versus Displacement data for the indentation test for modulus measurement	38
7.3	Graph of Force vs. Displacement ³² representing the Hertzian fit for the loading curve from the indentation test for modulus measurement	38

8.1.1	Raw data and Stress-Displacement plots for	41
(a-d)	Structure 1 (18 micron side x 53 micron height with small spacing)	
8.1.2	Visual indications of buckling and unbuckling	42
(A-G)	for Structure 1 (18 micron side x 53 micron height with small spacing)	
8.2.1	Raw data and Stress-Displacement plots for	46
(a-f)	Structure 2 (18 micron side x 53 micron height with medium spacing)	
8.2.2	Visual indications of buckling and unbuckling	48
(A-E)	for Structure 2 (18 micron side x 53 micron height with medium spacing)	
8.3.1	Raw data and Stress-Displacement plots for	51
(a-b)	Structure 4 (16 micron side x 53 micron height with small spacing)	
8.3.2	Visual indications of buckling and unbuckling	52
(A-E)	for Structure 4 (16 micron side x 53 micron height with small spacing)	
8.4.1	Raw data and Stress-Displacement plots for	55
(a-b)	Structure 5 (16 micron side x 53 micron height with medium spacing)	
8.4.2	Visual indications of buckling and unbuckling	56
(A-F)	for Structure 5 (16 micron side x 53 micron height with medium spacing)	
8.5.1	Raw data and Stress-Displacement plots for	59
(a-b)	Structure 6 (16 micron side x 53 micron height with large spacing)	

8.5.2	Visual indications of buckling and unbuckling	60
(A-G)	for Structure 6 (16 micron side x 53 micron height with large spacing)	
9.1	Schematic figure of a typical buckling strut	63
9.2	Log-log plot of stress (in KPa) vs. the dimensionless parameter $\pi^2 EI/L^2$	66

ABSTRACT

A large number of organisms in nature can adhere to and walk rapidly across a variety of surfaces. These organisms, like the Gecko, are found to possess efficient attachment mechanisms in which patterned surface structures interact with the profile of the substrate. The project undertaken seeks to provide an understanding of the working and guidelines for the design of synthetic, biologically inspired mimics. Samples representing microfibrillar mats are designed using an elastomer that is molded in a Silicon master fabricated by photolithography. A study of the mechanism of contact behavior and microbuckling on the samples is made. The buckling and unbuckling data are recorded from the indentation experiments performed on these samples. The values of the buckling as well as unbuckling stresses are found to vary with the density between the fibrils. The data observed are compared with those of buckling struts with classical boundary conditions.

Chapter 1

INTRODUCTION

Various organisms in nature have approached the challenge of controlled adhesion in a number of ways. Animals with widely varying body weight, such as flies, spiders and geckos can adhere to and walk rapidly along vertical walls as well as move upside-down on ceilings. This ability is caused by very efficient attachment mechanisms in which patterned surface structures interact with the profile of the substrate. The contacting surfaces in all such creatures have been found to be covered by fine patterns of fibrils and appear to have evolved the ability for re-applicable adhesion to a variety of surfaces [1-6]. Some animals secrete fluids (insects) in the contact area, whereas others do not (spiders, geckos). Therefore, different basic physical forces can be expected to contribute to the overall adhesion [2].

An extensive microscopic study has shown a strong inverse scaling effect in these attachment devices. Whereas dimensions in the microns of the terminal elements (setae) are sufficient for flies and beetles, geckos must resort to sub- μm devices to ensure adhesion [2, 3, 5].

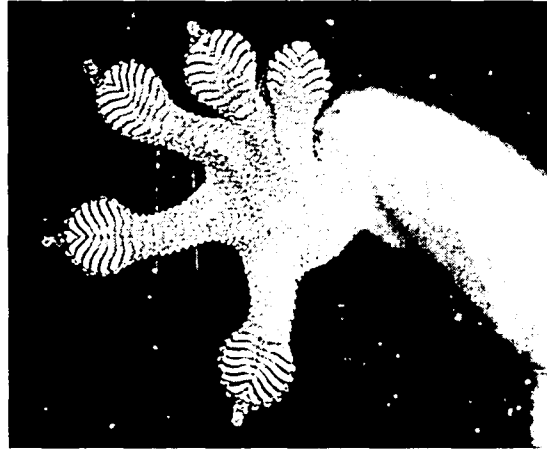


Figure 1.1: Lamellar structure of a Tree Dtella, *Gehyra variegata*
(Courtesy Museum Victoria)

The fact that various structures like these have evolved independently suggests that this kind of geometry has some universal benefits. Many unique properties of such biological structures have been noted in the literature. These include their ability to self-clean and be re-used as well as their mechanisms of directional adherence and controlled release [1-5]. The foot of a Tokay gecko (*Gekko gekko*) has about 5,000 setae per mm² and can produce 10 N of adhesive force with approximately 100mm² of pad area [2]. Therefore, the mimicry of these biological structures using synthetic materials has invoked a great deal of interest, with hopes that the mimic structures will have similar properties as those found in biology.

With a fibrillar design in common, different animals have evolved distinct variations. These variations include geometrical parameters such as fibril dimensions

and density, and other details such as hierarchical levels (if any) and flattened tip structures (spatulae) [1, 3, 5].

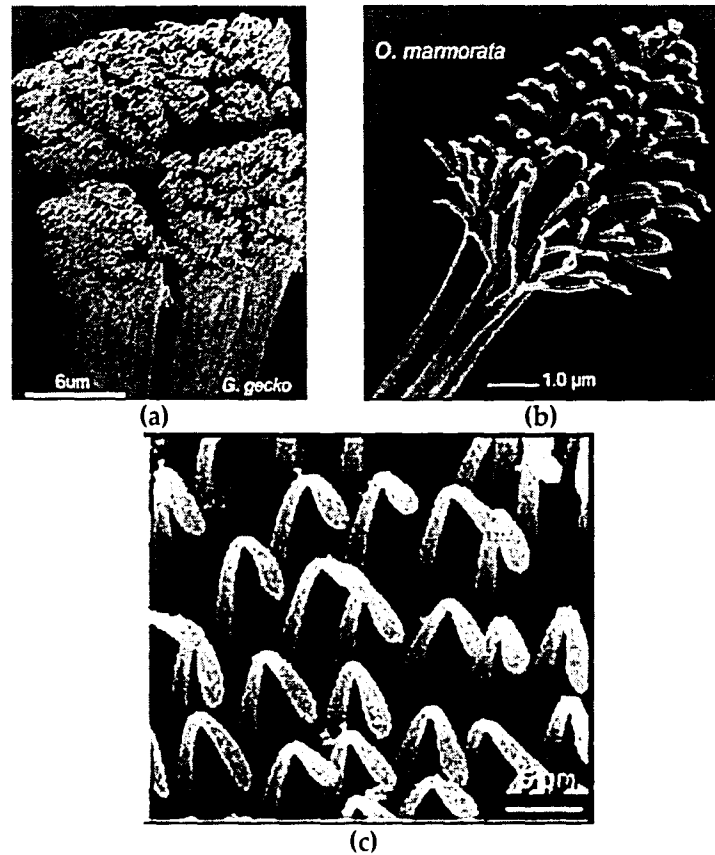


Fig 1.2: (a) Hierarchical fibrillar structures in *G. Gecko*, terminating in thin spatulae, courtesy N. Rizzo (DuPont), (b) Near-tip structure in *O. marmorata* courtesy N. Rizzo (DuPont). (c) Fibrillar and spatular structure in insects [5]

Clearly, the architecture is required to be designed and optimized carefully so that the structure may deliver the desired adhesive performance. The large amount of interest in the fibril design question is both to understand the working of the natural structures and to provide design principles and direction for their bio-mimicry.

Strong evidence has been presented that the adhesion of gecko setae is caused by Van der Waals interaction, although capillary forces due to the presence of a very thin layer of water cannot be ruled out [3]. Elements of contact mechanics have also been applied to this problem [7-12, 14-16]. The natural adhesive systems use these principles extensively and their study may facilitate their transfer into practical applications of synthetic mimics.

These synthetic mimics can enhance adhesive properties by use of fibrillar architecture, which has recently been demonstrated using micro-fabrication to pattern a polyimide film [13]. Experimental results by Hui et al. 2004 [8-9] show enhanced adhesion for synthetic polydimethylsiloxane (PDMS) fibrillar surfaces, as does recent work by Peressadko & Gorb (2004) for another elastomeric material. The largest 'adhesion force' measured ($\approx 200\mu\text{N}$ per setae) is from experiments performed predominantly under shear, whereas most theory and attempts to mimic the adhesive properties have been performed in normal interfacial separation (measured force for separation $\approx 10\text{--}40\mu\text{N}$ per setae). Gao et al. have recently explored some features of the performance in shear and have shown that by a combination of intrinsic adhesive properties and geometry one can obtain significant strength in shear.

The aim of the project undertaken is to provide an understanding and guidelines for the design of synthetic, biologically inspired mimics as well as to look at the mechanism of contact behavior and microbuckling.

There have been several attempts to fabricate fibrillar structures to mimic the biological ones using various techniques. We have fabricated well-defined fibrillar structures using microlithographic patterning techniques. Using such structures, a 16-fold increase in adhesion per unit area of actual contact has been observed as compared to a flat control. The actual adhesion, however, was still found to be less than that of a flat control [7-11].

Materials fabricated so far have been one-level structures that all have approximately uniform cross-sections and flat tips. The various contact and adhesion tests performed on these structures involved smooth glass or silicon substrates where roughness is small [7-9].

To explore the mechanisms of deformation in such structures, we consider a simple geometrical model of a microstructure consisting of an array of raised columns having square cross-section protruding from a backing film. The microstructure is typically fabricated by molding an elastomer, commonly

polydimethylsiloxane (PDMS), on a master fabricated using traditional optical lithography.

Fibrillar microstructures varying in size and density of the fibrils are designed and fabricated. Using these microfibrillar mats, we examine their behavior under compressive loading. In particular, we explore the phenomenon of fibrillar buckling and a previously observed distinct difference between buckling and unbuckling forces.

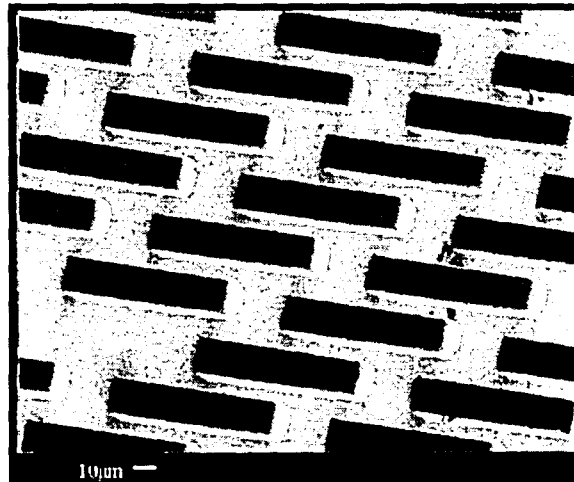


Fig 1.3: Fibrillar microstructure fabricated by molding polydimethylsiloxane (PDMS), on a Silicon master fabricated using photolithography.

We restrict our attention here to the simplest fibrillar structures for the sake of comparison of experimental data.

We start with a discussion on the development of the design of the fibrillar structures used for contact and adhesion experiments. The structures need to be designed such that the fibrils do not collapse and can sustain an amount of load enough to study the buckling and unbuckling of the various samples.

Chapter 3 explains the processes involved in making a photomask and the photolithography required to produce patterned silicon masters. It also describes the surface treatments performed on the masters to avoid the adhesion of PDMS to the master. The samples are typically fabricated by curing PDMS from liquid to elastomer using Si masters as described in chapter 4. The samples thus fabricated are viewed through a Scanning Electron Microscope and the actual dimensions are measured.

The experimental setup required for the indentation experiments to study the adhesive properties of the various structures designed and fabricated are described in chapter 6. The following chapter explains how the experimental setup is used to measure the modulus of the elastomer. The observations and inferences from the indentation experiments are shown in chapter 8. Chapter 9 compares these observed buckling and unbuckling stress values with those of struts with classical boundary conditions.

Chapter 2

DESIGN

In order to study the quantitative relationships between parameters of a fibrillar structure and resulting micro buckling behavior, we have designed structures comprising arrays of raised columns having square cross-section protruding from a base of the same material. These have been fabricated by curing liquid poly(dimethylsiloxane) (PDMS) to an elastomer on a silicon master fabricated using traditional optical lithography and etching techniques.

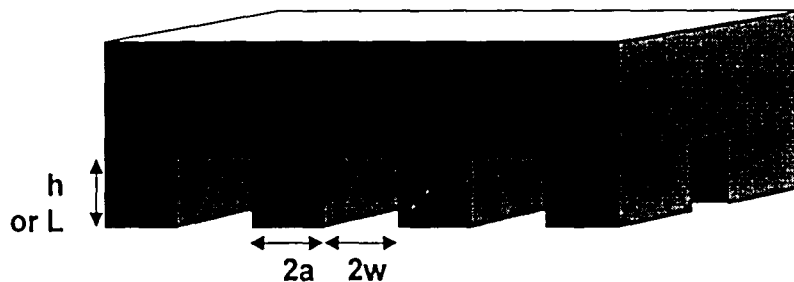


Figure 2.1: Dimensions of the microfibrillar mat.

Experiments by Biebuyck et al. have demonstrated that if the aspect ratio of the fibrils ($h/2a$) is too large the fibrils can buckle under their own weight (see Fig

2.2). Moreover, lateral collapse of neighboring fibrils can occur, where the capillary and other forces experienced by the fibrils are sufficiently large to cause them to come into contact. Once contact occurs, they may adhere to each other due to surface adhesive forces. These mechanisms are detrimental to adhesion since collapsed or buckled fibril bundles do not make good contact. Also, low aspect ratios can cause the recessed surfaces to come into contact with the substrate. The contact area may increase due to the action of surface forces near the edge of contact.

2.1 Design Calculations

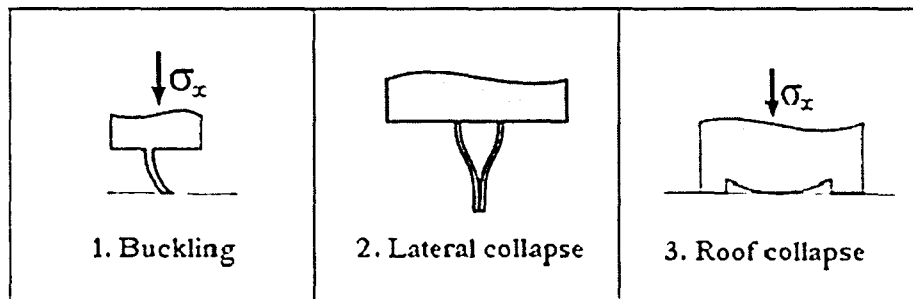


Figure 2.2: Idealized depictions of undesirable deformation modes. (Adapted from Hui et al, Langmuir 2002)

To prevent the three failure modes mentioned above for the geometry drawn in Fig 2.2, the conditions that must be satisfied are [10-11]

$$\frac{(-4\sigma_{\infty} w)}{(\pi E \times h)} \times (\pi E \times h) \times \left(1 + \frac{a}{w}\right) \cosh^{-1} \left[\sec \left(\frac{w\pi}{2(w+a)} \right) \right] < 1 \text{ ..(Roof collapse) - eqn. 2.1}$$

$$\frac{(-12\sigma_{\infty} h^2)}{(\pi^2 E \times a^2)} < \frac{1}{1+(w+a)} \quad \text{..... (Buckling) - eqn. 2.2}$$

$$\frac{h}{2a} \left(\frac{4\gamma_s}{3E \times a} \right)^{\frac{1}{4}} < \sqrt{\frac{w}{a}} \quad \text{..... (Lateral collapse) - eqn. 2.3}$$

Here, σ_{∞} is the uniform stress applied to the top of the sample.

$E^* \equiv E / (1-\nu^2)$ is the plane strain modulus of the sample material, where E is the Young's modulus and ν is the Poisson's ratio of the material.

Further, γ_s is the surface energy of the material, and $2a$, $2w$, and h are the dimensions of the features' width, spacing, and height, respectively (see Fig 2.1).

The fibrils need to be designed taking into consideration lateral collapse constraints. The aspect ratio needs to be maintained such that is not too large, which might cause the plates to collapse when loaded, or even under their own weight (buckling). Also, the minimum distances separating fibrils of various sizes considering lateral collapse constraints are calculated.

Samples studied in this work have been designed in the following way. Let s be the length of one side of the square cross-section of the fibril (ranging from 1 micron to 15 microns).

We calculated the required spacing to allow an aspect ratio $\left(\frac{h}{2a}\right) = 8$ for any given fibril size.

$$I = \frac{s^4}{12} \quad \dots \text{eqn 2.4}$$

γ_s is taken as 0.055 J/m² and E is assumed as 3.14 MPa

The critical spacing required to prevent the failure modes mentioned is calculated using equations 2.3 and 2.4 as

$$w_{critical} = h^2 \times \left(\frac{2\gamma_s s}{36EI}\right)^{\frac{1}{2}} \quad \dots \text{eqn 2.5}$$

The aim of the experiment includes studying fibrillar micro-structures of not just varying size but also various densities of fibrils. Hence, the structures are designed with 1, 2 and 3 times the critical distance required between the fibrils to prevent the failure modes discussed above.

2.2 Structure specifications

Following the conditions mentioned, the specifications for fibrillar structures of varying size ($2a$) and spacing ($2w$) are calculated as:

	spacing 1 (almost equal to critical spacing)	spacing 2 2 x spacing 1	spacing 3 3 x spacing 1
side ($s=2a$) micron	Small ($2w_1$) micron	Medium ($2w_2$) micron	Large ($2w_3$) micron
1	7	14	21
2	10	20	30
3	12	24	36
4	14	28	42
5	15	30	45
6	17	34	51
7	18	36	54
9	21	42	63
11	23	46	69
13	25	50	75
15	27	54	81

Table 2.1: Specifications for fibrillar structures of varying size ($2a$) and spacing ($2w$)

Chapter 3

PROCESSING

This section describes the processes required to produce Silicon masters. The masters to create the samples are prepared using the process of photolithography. This process is used because it affords excellent control over the shape and size of the objects it creates, and because it can create patterns over an entire surface simultaneously. Its main disadvantages are that it requires a substrate to start with, it is not very effective at creating shapes that are not flat, and it can require extremely clean operating conditions.

In brief, the process of photolithography can be explained starting with the production of a photomask (see Fig. 3.1).

- (a) The Si master with a layer of photoresist is exposed to the radiation through the photomask.
- (b) The degraded areas of the photoresist are removed exposing the Si wafer.
- (c) The wafer then undergoes a Reactive Ion etch which forms the required relief pattern on it.

(d) The resist is burned away in a plasma chamber leaving behind a patterned Si master.

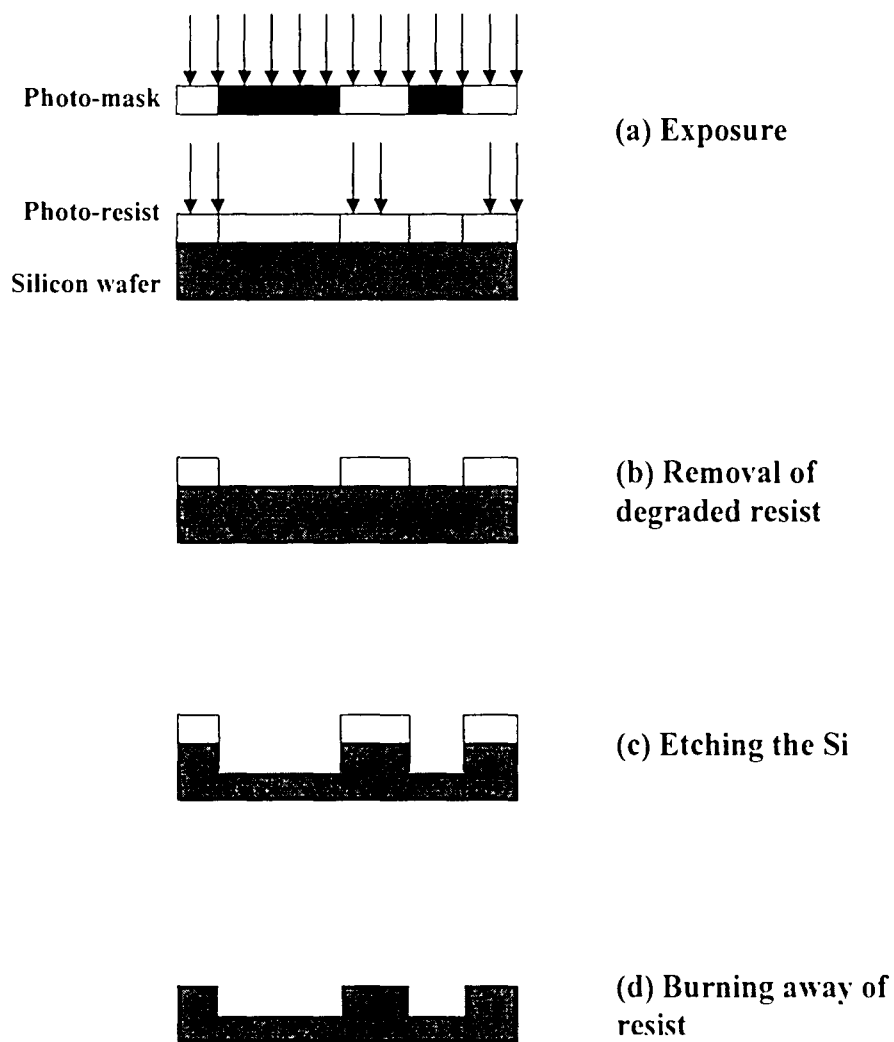


Figure 3.1: Patterning Si masters using Photolithography

The processes involved in photolithography are explained in detail in 3.1 and 3.2.

3.1 Photo-mask processing

A photo-mask is typically a transparent fused quartz blank imprinted with a pattern defined with chrome metal. The design (created using design software such as L-EDIT®, Tanner Research, Inc.) defining the pattern is fed into a photolithography stepper and the mask selected for exposure. The photo-mask is created by a photographic process and developed onto a glass substrate. The feature size is limited by the diffraction limit and depends on the size of the wavelength of light used to illuminate the mask.

During the process of exposure, the resist undergoes a chemical reaction. According to the chemical composition of resist, it can react in two manners when the surface is exposed to the light. The action of the light on positive resist causes exposed areas to become polymerized. Negative resist has the reversed property. After the developing process, negative mask remains as model resist. For positive photosensitive varnishes, acetone, trichloroethylene and phenol-based solvents can be employed. For negative resists, methyl ethyl ketone or the methyl isobutyl ketone are generally employed.

3.2 Making the Silicon master

Deep Reactive Ion Etch was used to make silicon masters. A layer of photoresist -- a chemical that hardens or degrades when exposed to light (often ultraviolet) -- is applied on top of the Si wafer. The photoresist is selectively "hardened" or "degraded" by illuminating it in specific places.

For this purpose, the photomask is used together with an illumination source to shine light on specific parts of the photoresist defining the pattern required.

Before the photo-resist is applied to the substrate, the surface is cleaned to remove any traces of contamination from the surface of the wafer such as dust, organic, ionic and metallic compounds. The cleaned wafer is subject to priming, to aid the adhesion of the resist to the surface of the substrate material.

A resist is applied to the surface using a spin-coating machine. A small quantity resist is dispensed in the centre of the spinning wafer. The rotation causes the resist to be spread across the surface of the wafer with excess being thrown spun off. Preparation of the resist is concluded by a pre-bake, where the wafer is a gently

heated in a convection oven and then a hotplate to evaporate the resist solvent and to partially solidify the resist.

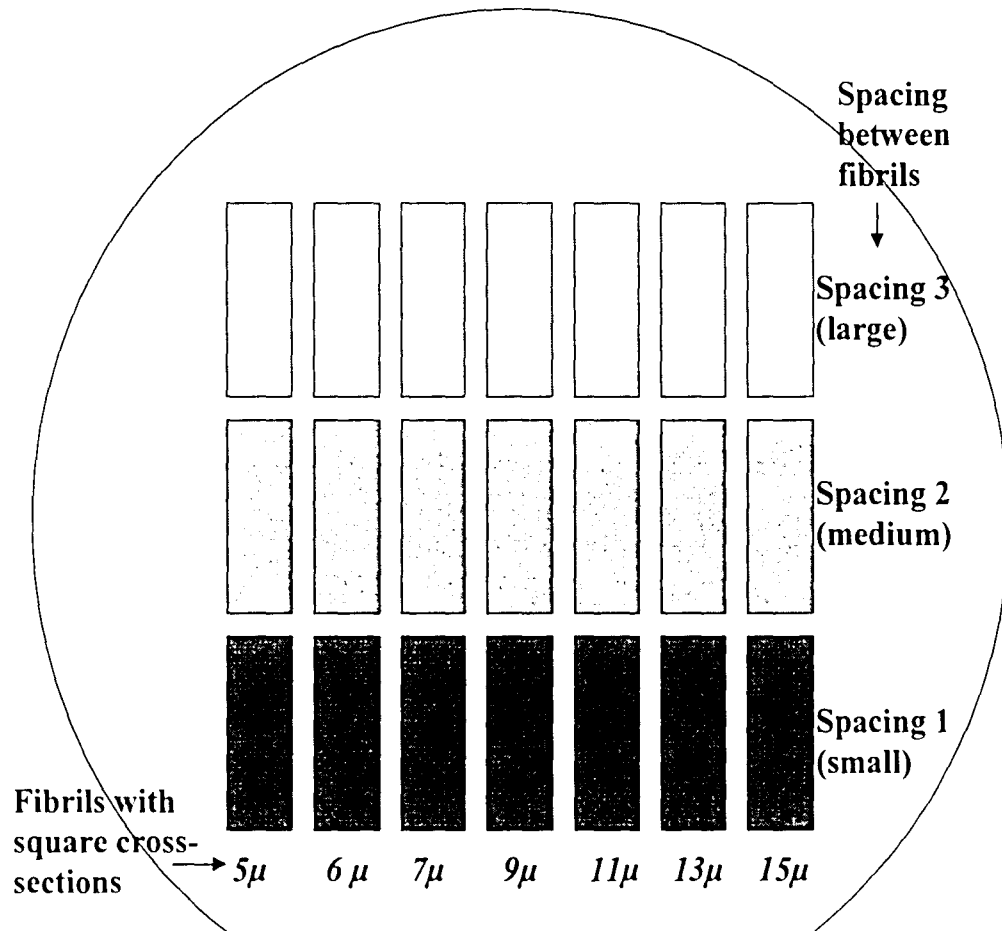
The pattern is transferred from the photo-resist to the Si using Deep Reactive Ion Etch process. Finally, the resist is burned away leaving behind a patterned Si wafer. Such patterned Si wafers are used to mould the elastomer (PDMS) into the required patterns.

Steps involved:

1. Cleaning the wafer: Si wafer (4inch diameter) was cleaned using an isopropyl alcohol rinse.
2. Wafers are liquid primed with P-20 (20% HMDS) primer. Primer is applied over the entire wafer, allowed to remain for 10 seconds, and then spun dry at 4000rpm for 35 seconds.
3. The Shipley 1818 photo-resist is dispensed in the middle of the wafer and spun immediately at 4000rpm for 35 seconds.
4. The wafers are then pre-baked at 115 C for 60 seconds on a hot plate to remove solvent from the resist.
5. The wafers are exposed in the GCA AS200 Auto-step 5X I-line stepper.

6. These are developed for 1 minute in AZ 300MIF for 60 seconds.
7. The developed samples are rinsed with De-Ionized H2O and dried with N2.
8. The pattern is transferred from the photo-resist to the Si using Deep Reactive Ion Etch in the Unaxis 770 for 128 loops. Depth is approximated at 56 microns.
9. Aura or Glen 1000 oxygen plasma cleans until all resist is "burned" away.

Photolithographic masters were fabricated with various isolated regions containing square relief patterns of differing sizes and densities.



. Fig 3.2: Schematics of relief pattern on 4" Si Master for molding fibrillar structure with varied sizes and densities

3.3 Treating the Si Master & Glass slides

The fibrillar samples are fabricated by curing liquid to an elastomer, poly(dimethylsiloxane) (PDMS), on the silicon master fabricated as described in the previous section. The surface on the silicon master requires surface treatment to reduce adhesion with the PDMS so as to facilitate its removal after curing to a solid. The samples can be peeled from the master if there is sufficiently low adhesion of the elastomer to the master. To ensure low adhesion to the elastomer, a self-assembled monolayer is created on the surface of the master. The PDMS was poured on the mould in fluid form and cured in an oven to harden it. Once cured, the PDMS was manually peeled from the master.

To create a self-assembled monolayer, the surfaces of the master and the glass slides coming into contact with the PDMS are cleaned. After oxygen plasma treatment, the surfaces are exposed to the silane (n-hexadecyltrichlorosilane) under vacuum. Self assembled monolayers of n-hexadecyltrichlorosilane are formed on the surface. The low adhesion of the PDMS to the master allows the sample to be peeled undamaged from the master.

Under ideal conditions, the surfaces will be hydrophobic and the peeled sample is an exact negative replica of the master.

Steps involved:

1. The patterned Si Wafers and glass slides are immersed in piranha solution (30% of 50% H₂O₂ + 70% of 90% sulfuric acid) for 30 minutes.
2. Rinse slides and wafers with DI water 3-4 times.
3. Dry with N₂ gas.
4. Place in oxygen plasma chamber at a chamber pressure of 200 mTorr and plasma power of 7.16 W for 3-4 runs.
5. Liquid n-hexadecyltrichlorosilane contained in a dish is placed in a vacuum chamber for about 60 minutes until bubbles are removed from solution.
6. Slides and wafers are placed over the dish in vacuum for 90 minutes.
7. A self assembled monolayer of n-hexadecyltrichlorosilane is formed on the glass slides and Si wafers making the surfaces hydrophobic.

Chapter 4

FABRICATION OF PDMS FIBRILS

After the silicon masters are patterned by photolithography, the fibrillar structures required were fabricated by the curing of liquid to elastomer using the masters. The elastomer used is poly(dimethylsiloxane) (PDMS) (Sylgard 184 , Dow Chemicals) in a ratio of 10:1 (rubber base:cure). The Si masters are treated as explained in the previous section and cut to required sizes. The rubber base and curing agent are mixed in the required ratio. The silicone mixture was out-gassed under vacuum for 30 minutes before applying to the master. This mixture is poured over the treated masters and covered with a treated glass slide. The masters and the cover glass slides are separated by feeler gauges according to the required thickness of the backing film. This arrangement is placed in a vacuum oven to cure the mixture. The cured sample is manually peeled from the master.

Steps involved:

1. The patterned Si Wafer is marked with a diamond scribe to fracture it to roughly the same size as a glass microscope slide ~ 3" x 1"
2. PDMS monomer and curing agent are mixed in the ratio 10 to 1 with a pipette.
3. The mixture is placed in a vacuum chamber (house vacuum) for 30 minutes to remove bubbles.
4. Feeler gauges are placed at both ends of the master to control the thickness of the PDMS film.
5. The PDMS mixture is poured over the treated master carefully and noticeable bubbles are popped.
6. A treated glass slide is used as a cover and clipped to the master and the feeler gauges.
7. The mixture is then cured in the vacuum oven (house vacuum) at 80 C for 60 minutes.
8. The sample from the vacuum oven is cooled at room temperature for about 60 minutes.
9. Feeler gauges are removed and the sample is buried in dry ice for about 60 minutes.
10. Cover glass is removed and sample is peeled off the master.

Chapter 5

SCANNING ELECTRON MICROSCOPE VIEWS

Scanning electron microscopy (SEM) pictures of Si masters, and as-produced fibrillar structures are shown in figures 5.1 – 5.5

Figure 5.1 shows the surface of a Si master. The square cross-sections etched into the wafer appear to have slightly rounded edges. Figure 5.2 shows the length of the trench. Also, the cycles during the etching cause the trench to taper slightly.

Figures 5.3 to 5.5 show the fabricated fibrillar structures. The structures have square cross-sections with slightly rounded edges and the lengths of the fibrils are well-controlled. The sample shown has medium spacing. No lateral collapse was noticed. This proves that the design calculations to avoid failure were successful.

The actual dimensions were calculated by measuring the dimensions of a large number of (between 15 and 50) fibrils, comparing these with the measurements from the SEM images and deducing the dimensions of single structures.

5.1 SEM views of Silicon master

Figure 5.1:

Surface of Silicon master with square trenches.

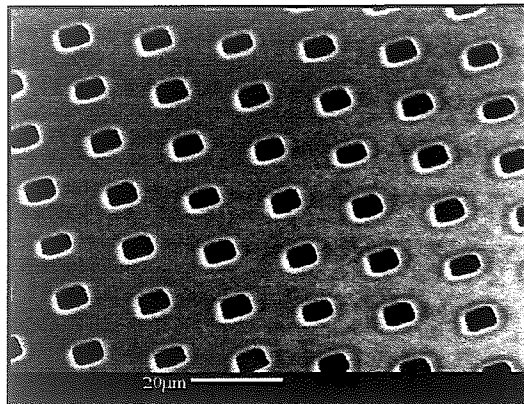
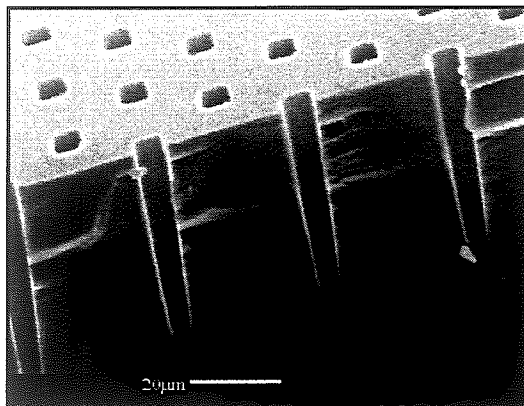


Figure 5.2:

Length-wise section of trenches in the Silicon master.



(Courtesy: N. J. Glassmaker)

5.2 SEM views of Fibrillar sample

Figure 5.3:

Single fibril – Top view

Actual measurements:

18 micron x 18 micron cross-section

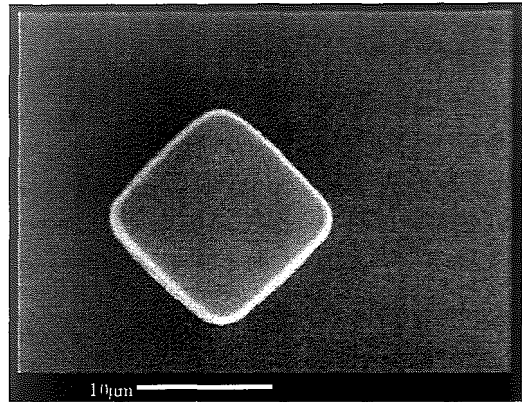


Figure 5.4:

Top view of sample

Spacing: medium

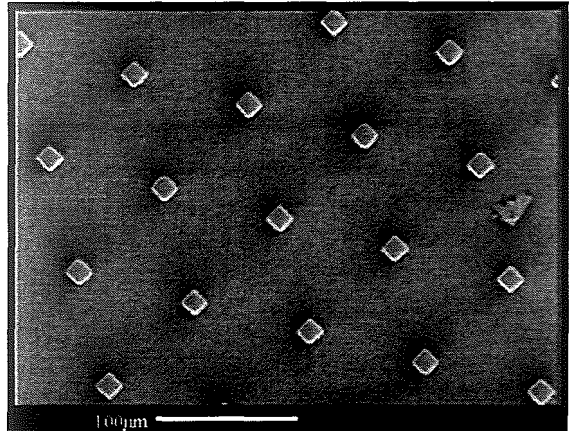
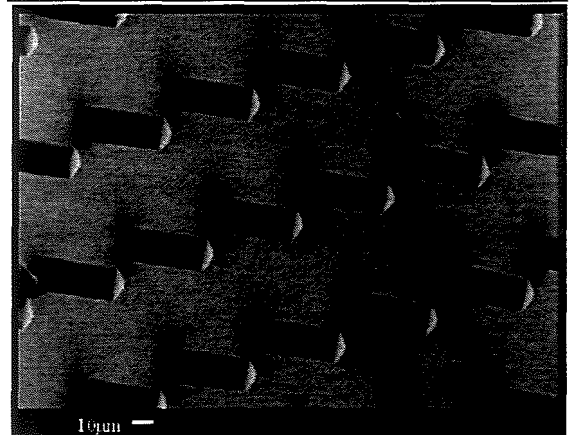


Figure 5.5:

Sample tilted at 60 degrees

Actual height of fibrils:

53 microns



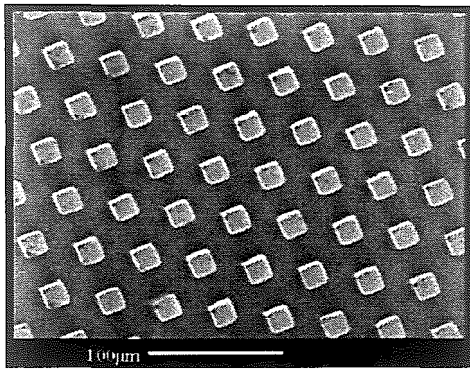
5.3 Sample structures tested

Structure	Fibril side designed	spacing
In microns		
1	15	small
2	15	medium
3	15	large
4	13	small
5	13	medium
6	13	large

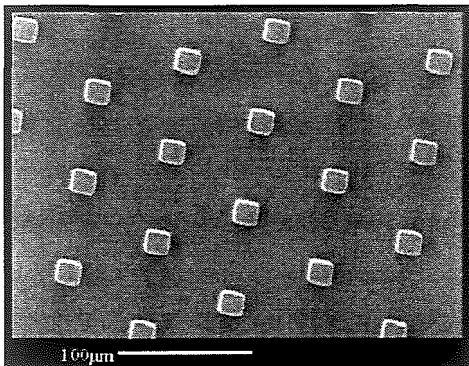
Table 5.1: Structures with fibril cross-section dimensions and spacing as designed

Structure	Fibril side measured	Fibril height measured	spacing
	microns	microns	
1	18.2	53	small
2	18.8	53	medium
3	18.2	53	large
4	16.5	53	small
5	16.3	53	medium
6	16.3	53	Large

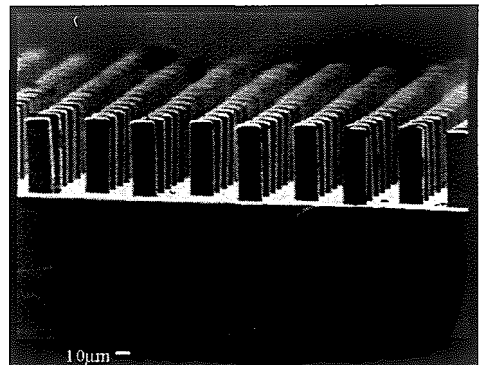
Table 5.2: Structures with fibril dimensions and spacing as measured



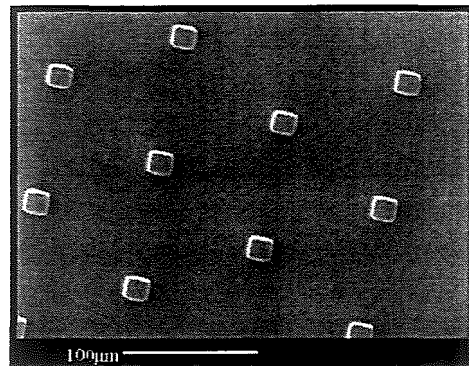
(a)



(b)



(c)



(d)

Fig 5.6 : Structures with fibrils having cross section dimensions of 18x18 microns and 53 microns in height : (a) Fibrils with small spacing: Top view
(b) Fibrils with medium spacing : Top view
(c) Fibrils with medium spacing : Side view
(d) Fibrils with large spacing : Top view

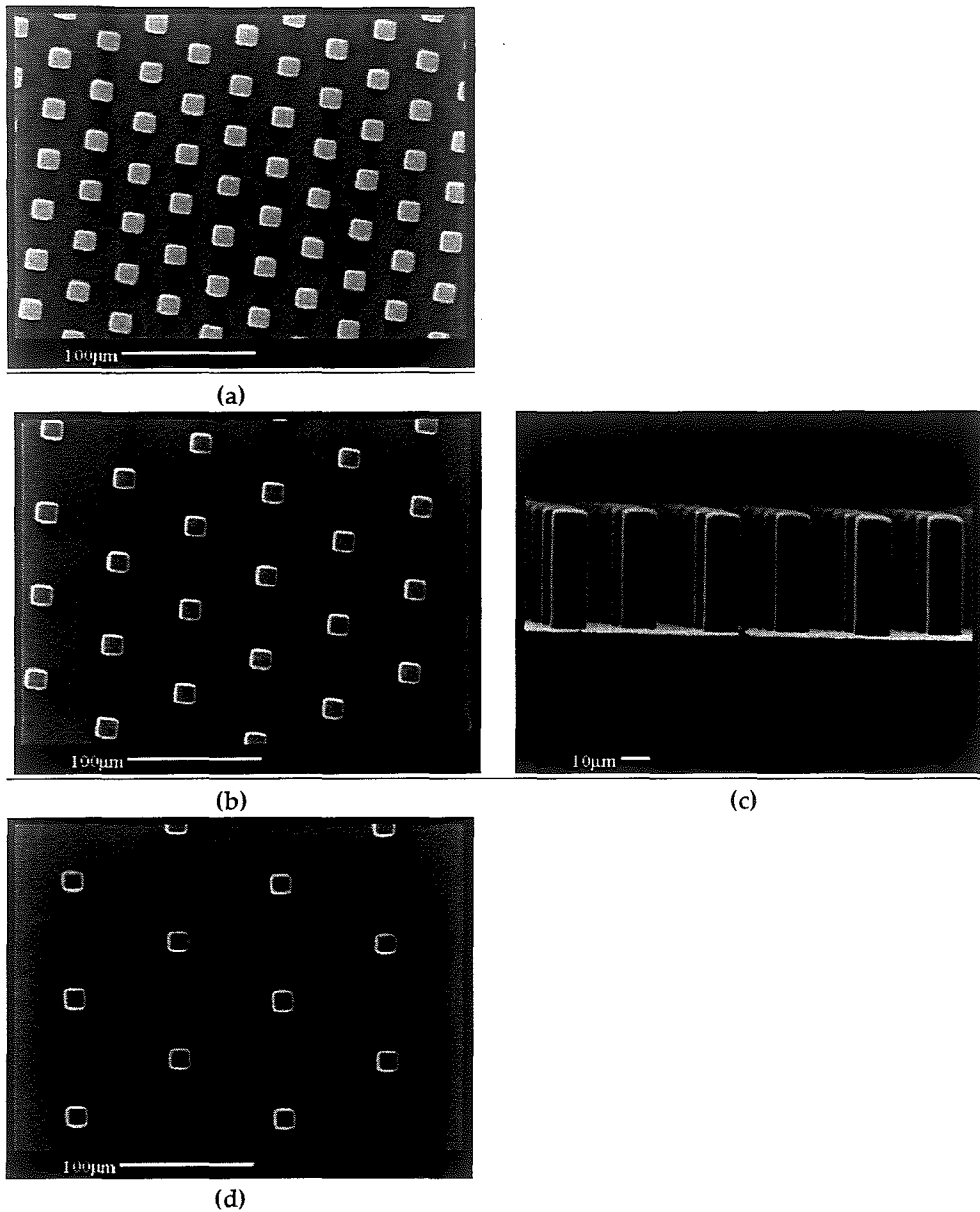


Fig 5.7 : Structures with fibrils having cross section dimensions of 16x16 microns and 53 microns in height (a) Fibrils with small spacing: Top view
(b) Fibrils with medium spacing : Top view
(c) Fibrils with medium spacing : Side view
(d) Fibrils with large spacing : Top view

Chapter 6.

EXPERIMENTAL SET-UP

To explore the mechanisms of adhesion, contact experiments were performed on the samples, where the specimen was placed on a glass slide and viewed with an inverted microscope during compression and retraction of the samples.

The specimen was placed on a glass slide with fibrils placed in contact with the glass slide and viewed with the inverted microscope (see Fig 6.1). It was loaded under displacement control, with concurrent force measurement via a load cell. The deformations were observed optically with the inverted microscope while load-displacement data was being acquired. The set-up ensured that the load is uniformly applied to the sample.

As shown in Fig 6.1, loading was applied via a flat piece of glass, slightly larger than the sample piece, with the spherical glass indenter. Displacement was monitored via a linear variable differential transformer sensor, and a load cell (50g or 150g max. load) attached in series to the vertical motor assembly measured the total applied force. The load-unload data were recorded for each pattern.

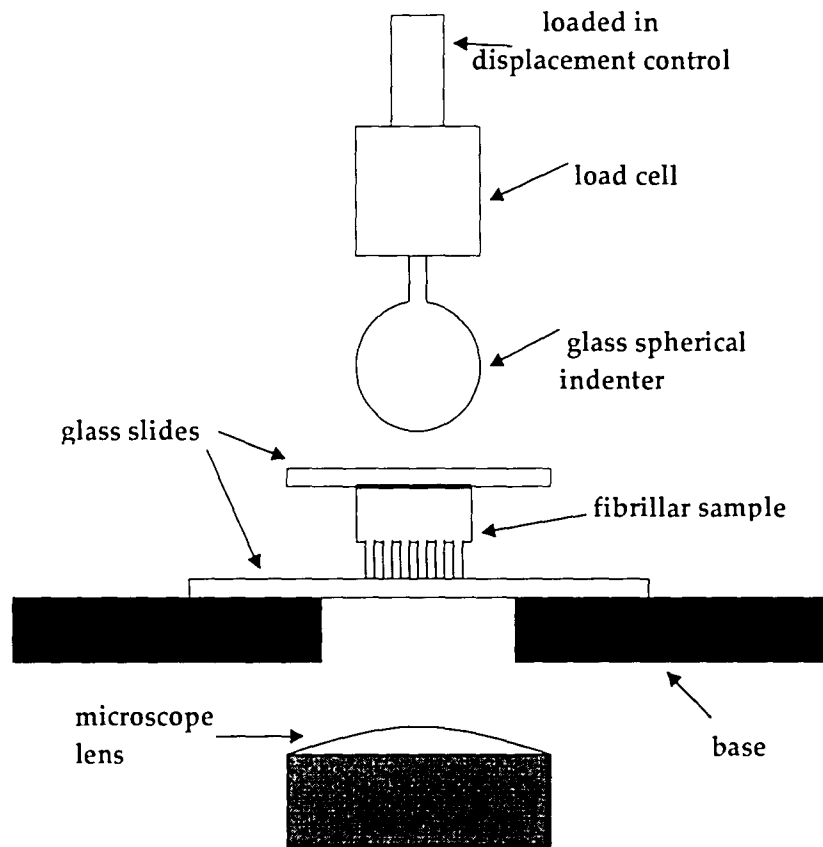


Figure 6.1: Schematic representation of experimental setup for indentation experiments (adapted from Glassmaker et al, 2004)

The sample is placed with the fibrils in contact with the glass slide. When viewed through the microscope, the dark areas represent areas in contact (see Fig 6.2) and the bright areas represent parts not in contact with the glass slide.

Initially, a circular contact is formed between the end of the rounded fibril and the substrate. On loading, this contact increases until the entire tip of the fibril is in contact with the glass slide. When the loading reaches a critical level, the fibril buckles and the interface loses contact. The load at this point is measured as the buckling load.

On unloading the converse occurs. The point where the fibril unbuckles is recorded as the load required for unbuckling. The direct visualization allows one to associate features in the force-displacement trace with physical events such as buckling and un-buckling. Consistent with previous theoretical work [11], the buckled region at the same total applied force is larger during unloading than during loading.

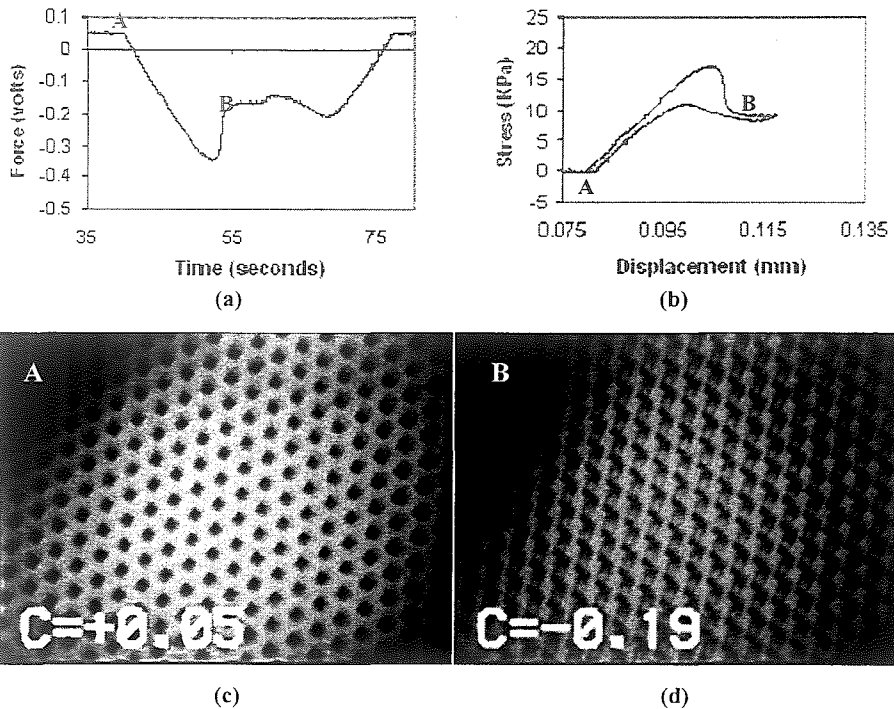


Fig 6.2: (a) Raw data representing force vs time graph for the sample. (b) Stress vs displacement graph for the sample. (c) Sample with tips of the fibrils in contact with the glass slide. (d) Sample with fibrils in buckled state. Figures A and B visually represent points A and B on the graphs.

Chapter 7.

MODULUS MEASUREMENT

7.1 Experimental Set-up

The elastic modulus of the PDMS used in this study was determined using the Johnson-Kendall-Roberts (JKR) contact test [12]. Specifically, we impinge the featureless area of the stamps with a ~4 mm diameter glass sphere (without the intervening glass plate) in a separate experiment.

Spherical indentation allows one to extract an effective modulus and an effective work of adhesion. A flat PDMS specimen was subject to indentation at the rate 0.005 mm/s to a depth of 150 microns. The experiment consisted of a loading and unloading step.

A circular contact region increases as the depth of indentation is increased, along with an increasing compressive force. In the loading step, there is an increase in the compressive force with increase in the downward displacement of the spherical

indenter. Conversely, the unloading step consists of a decrease in the force with upward displacement of the indenter.

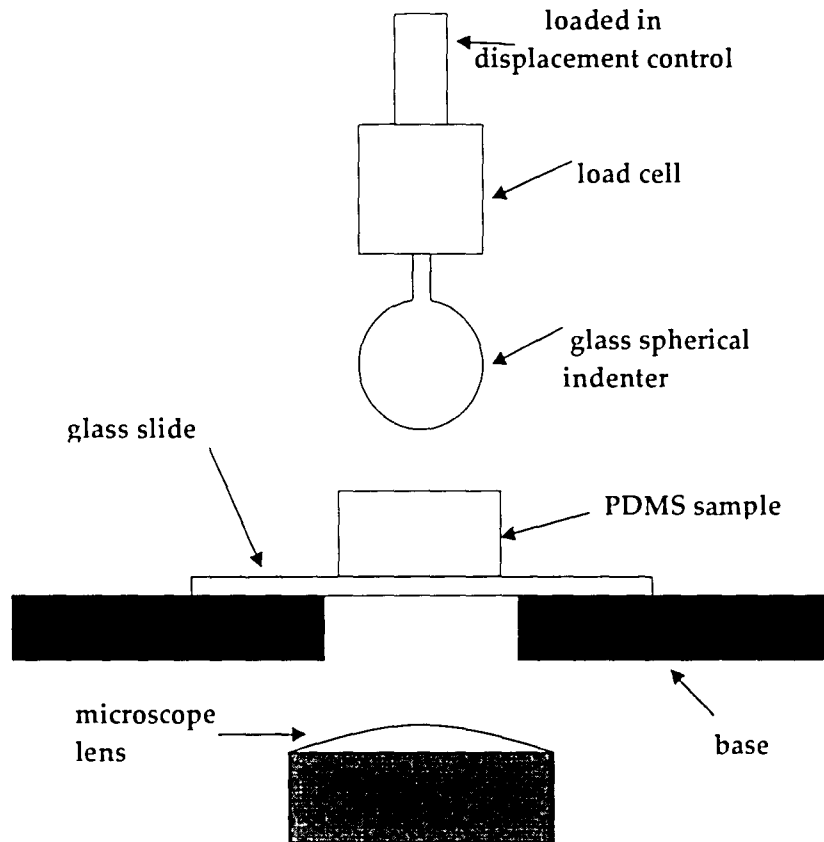


Fig 7.1: Schematic representation of experimental setup for modulus measurement.
(Adapted from Glassmaker et al, 2004)

Figure 7.2 show the load (F) versus displacement (δ) data for the indentation test. This shows that the loading and unloading curves nearly coincide. This result

reveals that the PDMS is almost purely elastic so that bulk viscoelastic effects can be neglected.

7.2 Calculations and plots

The elastic modulus is calculated by noting that, for sufficiently large load point displacement δ , the load-displacement relation is well approximated by the Hertz contact theory [12, 16], i.e.,

$$F = 4E^* \times \sqrt{R} \times \frac{\delta^{\frac{3}{2}}}{3} \quad \text{-eqn 7.1}$$

where R is the radius of the sphere. In this case, the radius is measured as 4.062mm.

The plane strain modulus E^* is defined as

$$E^* \equiv E / (1 - \nu^2) \quad \text{-eqn 7.2}$$

with the Poisson's ratio $\nu = 1/2$ for PDMS.

$$\text{So, } E = E^* (1 - \nu^2) \quad \text{-eqn 7.3}$$

The graph of Force v/s displacement^{3/2} is plotted and E is calculated from the slope.

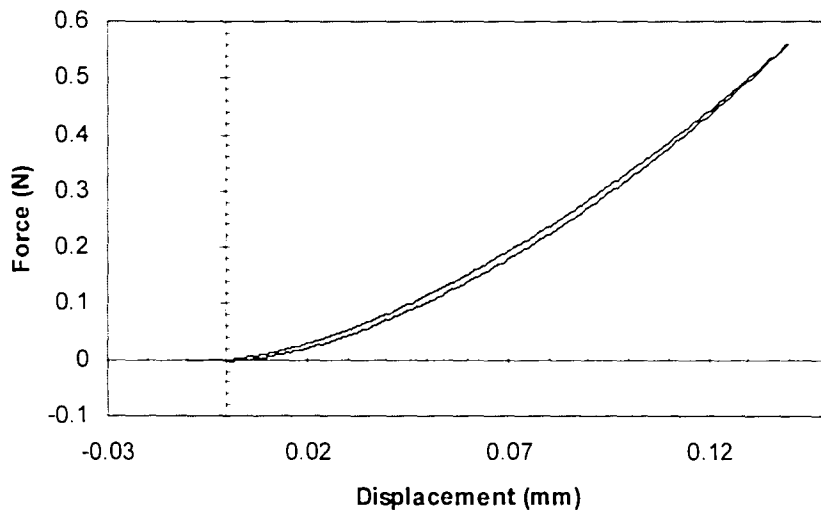


Figure 7.2: Load (F) versus Displacement (δ) data for the indentation test

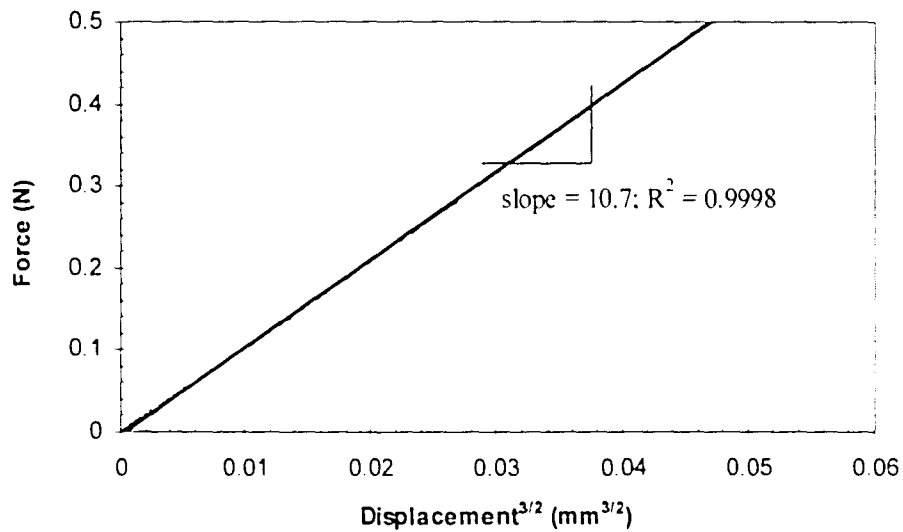


Figure 7.3: Graph of Force (N) vs Displacement^{3/2} represents the Hertzian fit for the loading curve from the indentation test

The result of the Hertzian fit is shown in Figure 7.3. Since the loading curve gave a better fit, we have used the elastic modulus obtained from the loading curve for the calculations here; $E = 2.98 \text{ MPa}$.

Chapter 8.

EXPERIMENTAL OBSERVATIONS AND MEASUREMENTS

The structures mentioned in section 5 are used for indentation experiments. The samples were placed with fibrils on a glass slide with a self assembled monolayer. Glass covers are used between the spherical indenter and the samples.

Experiments were performed at various velocity rates of the indenter, ranging between 0.02 mm/s and 0.25 mm/s, and each experiment consisted of a loading and unloading step. Load-displacement curves were acquired at the various rates with the visual information captured by a video recorder. Results were substantially independent of loading rate.

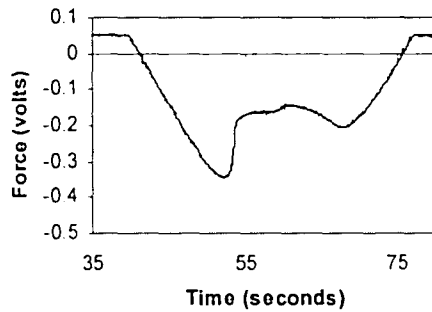
The following are examples of results of measurements.

8.1 Structure 1: 18 micron side x 53 micron height (small spacing)

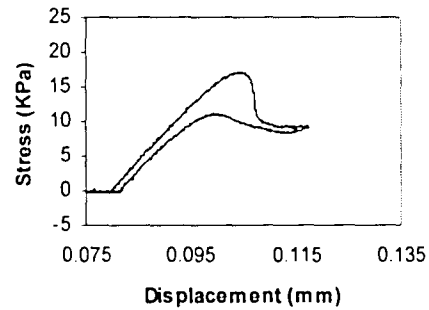
The approximate area of the sample used for experiments is 15mm x 15mm.

8.1.1 Raw Data and Stress-Displacement plots

Trial 38:

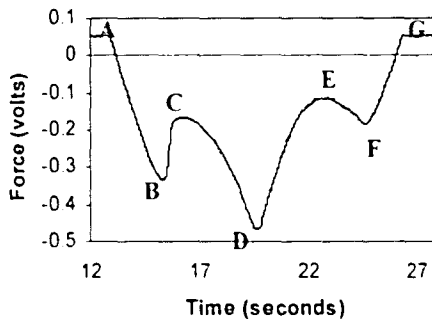


(a)

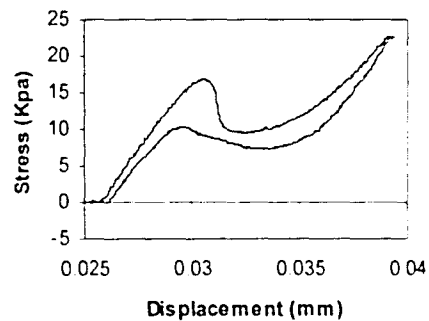


(b)

Trial 43:



(c)

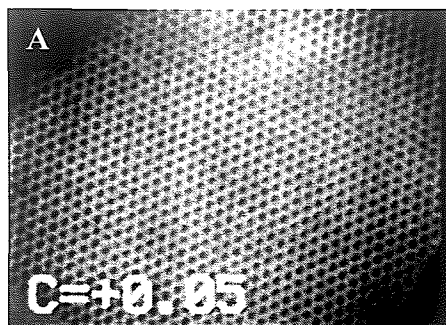


(d)

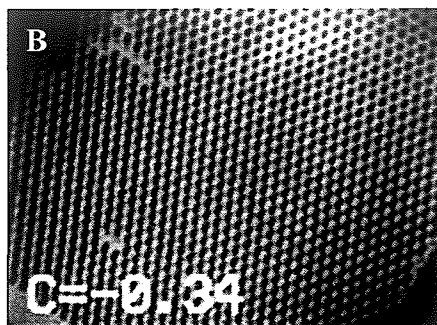
Fig 8.1.1: (a) Raw data representing force vs time graph for the sample during trial 38. (b) Stress vs displacement graph for the sample for trial 38. (c) Raw data representing force vs time graph for the sample during trial 43. (d) Stress vs displacement graph for the sample for trial 43.

8.1.2 Optical Micrographs:

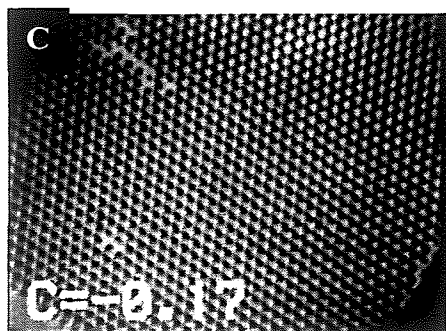
The optical micrographs below correspond to the points in the graph for trial 43.



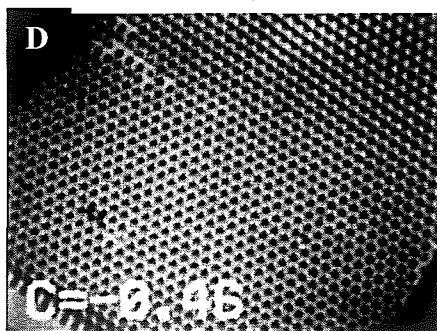
A. Fibrils in contact with the glass slide



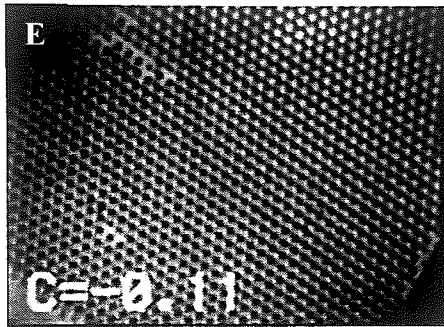
B. Fibrils starting to buckle



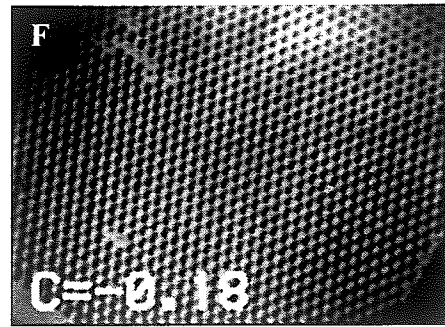
C. Fibrils in buckled state



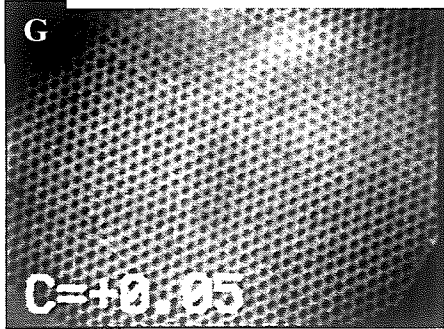
D. Fibrils in buckled state



E. Fibrils in buckled state



F. Fibrils starting to unbuckle



G. Fibrils in unbuckled state

Figures 8.1.2 (A-G): Visual indications of buckling and unbuckling for sample

8.1.3 Observations

Point A represents the situation where load is not applied to the sample. This point is represented as the portion of the graph that is parallel to the x-axis. There is an increase in the downward displacement of the indenter without any change in stress in the system. The indenter has just come into contact with the sample.

EXPERIMENTAL OBSERVATIONS AND MEASUREMENTS

The point B represents the point where the cross-sections of the fibrils lose contact with the glass slide. The fibrils are said to have buckled. There is a distinct dip in the graph. The compressive stress increases with increase in displacement of the indenter. As the indenter moves downward, the displacement of buckled fibrils increases. The stress applied on the sample at B is recorded as the critical buckling stress for the sample.

The buckling starts at B and at C the fibrils appear to have buckled completely. After this point, the fibrils remain in buckled form. From B to C, there is a slight decrease in stress and after C, the stress increases again.

The graph continues this trend until the indenter reverses direction of motion at D, starting the retracting part of its loading cycle. Now the stress decreases with upward displacement.

At point E, the fibrils appear to unbuckle. The cross-sections of the fibrils come into contact with the glass slide and appear dark again. As the fibrils unbuckle, there is a slight increase in stress from E to F. As expected from earlier theoretical work, the stress at buckling is observed to be considerably larger than the stress at unbuckling.

EXPERIMENTAL OBSERVATIONS AND MEASUREMENTS

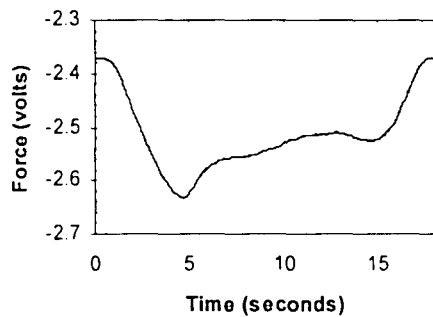
In trial 43, there is a greater displacement of the indenter as compared to trial 38. The shape of the force-time graphs and the stress-displacement graph change due to the variation in the indentation. After the buckling is observed in the graph, the force increases with time until the indenter starts moving upward.

8.2 Structure 2: 18 micron side x 53 micron height (medium spacing)

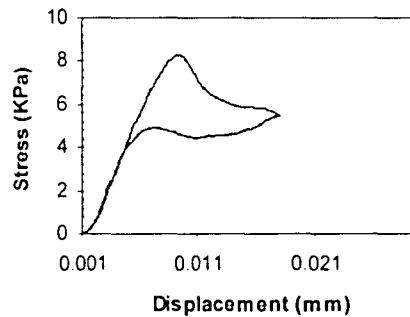
The approximate area of the sample used for experiments is 13mm x 13mm.

8.2.1 Raw data and Stress-Displacement plots

Trial 9:

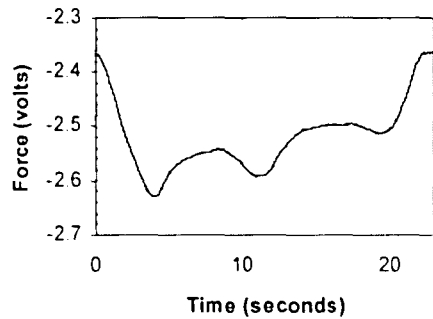


(a)

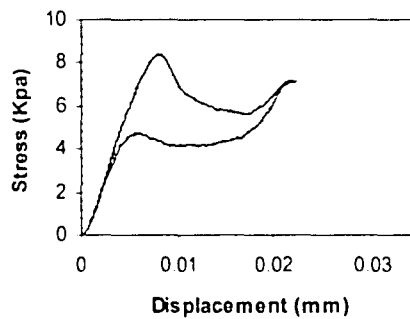


(b)

Trial 6:



(c)



(d)

Trial 5:

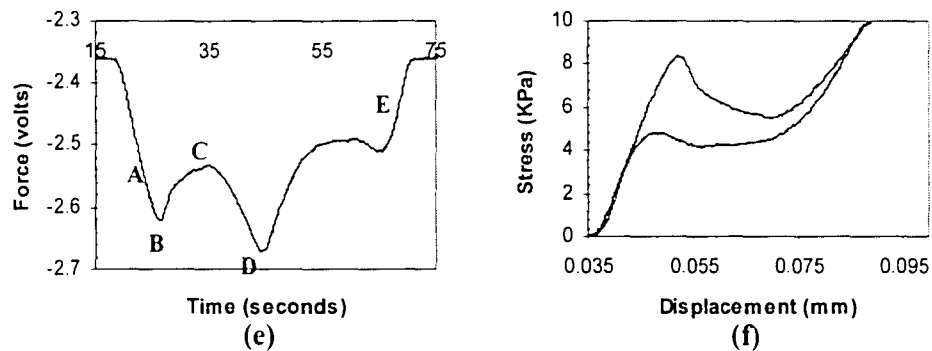


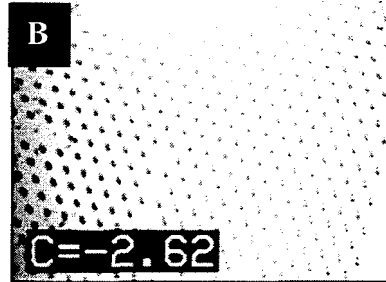
Fig 8.2.1: (a) Raw data representing force vs time graph for the sample during trial 9. (b) Stress vs displacement graph for trial 9. (c) Raw data representing force vs time graph for the sample during trial 6. (d) Stress vs displacement graph for trial 6. (e) Raw data representing force vs time graph for the sample during trial 5. (f) Stress vs displacement graph for trial 5.

8.2.2 Optical Micrographs:

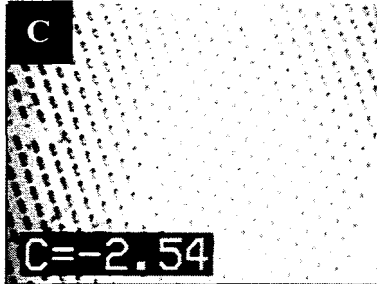
The optical micrographs below correspond to the points in the graph for trial 5.



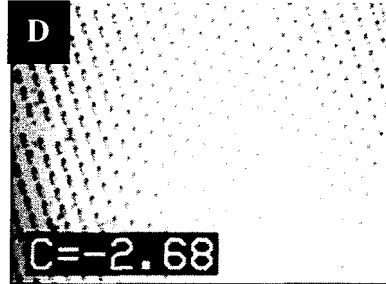
A. Fibrils in contact with glass slide



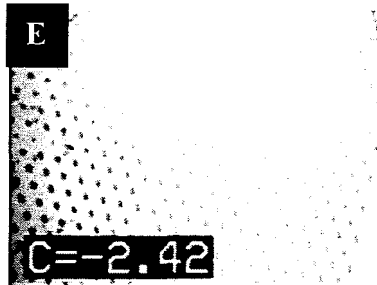
B. Fibrils starting to buckle



C. Fibrils in buckled state



D. Fibrils in buckled state



E. Fibrils in unbuckled state

Figures 8.2.2 (A-E): Visual indications of buckling and unbuckling for the sample

8.2.3 Observations

Before point A, the sample is under stress. The compressive stress in the system increases with downward displacement of the indenter. Although load is being applied to the sample, the fibrils haven't buckled as yet. The point B represents the point where the cross-sections of the fibrils lose contact with the glass slide and the fibrils start to buckle. B is recorded as the critical buckling stress for the sample. The compressive stress increases with increase in displacement of the indenter, the fibrils buckle further as the indenter moves downward. The graph between B and C is not as sharp as seen in the previous sample (with less space between the fibrils). The buckling of the fibrils seems less abrupt as compared to the earlier sample.

The buckling starts at B and with the slight decrease in stress as observed before; the fibrils appear to have buckled completely at C. After this point, the fibrils remain in buckled form till point D. The graph continues this trend until the indenter rises at D. Now the stress decreases with upward displacement. At point E, the fibrils appear to have unbuckled. The cross-sections of the fibrils come into contact with the glass slide and appear dark again. The various trials show the variation in the shapes of

EXPERIMENTAL OBSERVATIONS AND MEASUREMENTS

the graphs with increase in indentation. The critical stresses at buckling and unbuckling are comparable in all the trials.

Stress at buckling: 8778.4 N/m²

Stress at unbuckling: 4811.33 N/m²

8.3 Structure 4: 16 micron side x 53 micron height (small spacing)

The approximate area of the sample used for experiments is 13mm x 13mm

8.3.1 Raw data and Stress-Displacement plots

Trial 17:

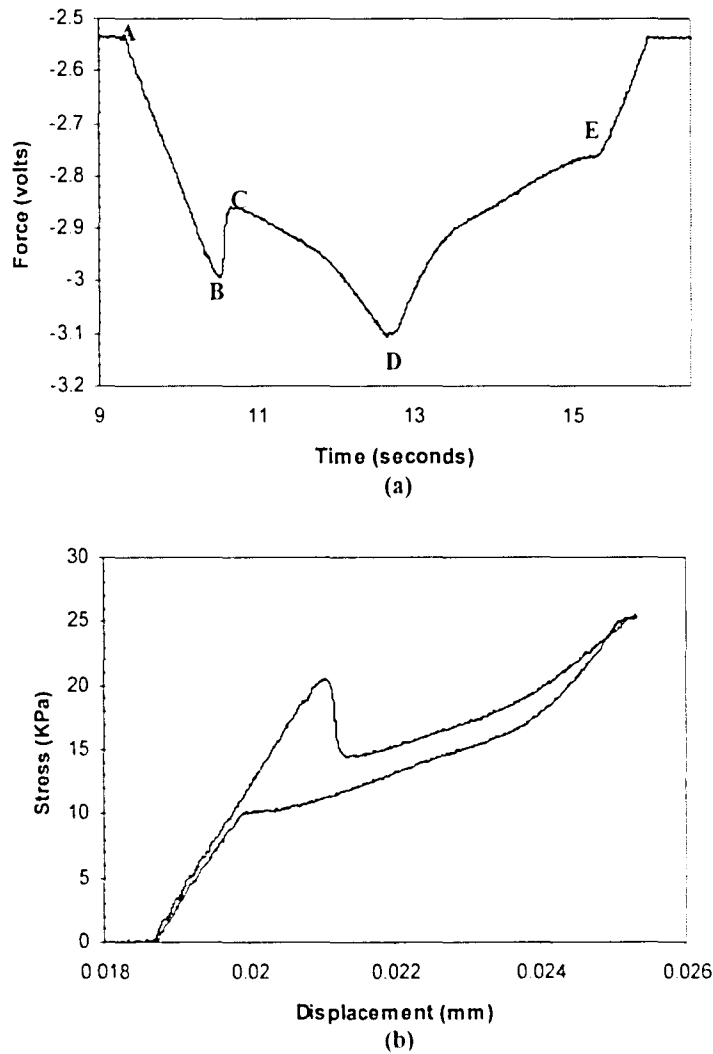


Fig 8.3.1: (a) Raw data representing force vs time graph for the sample during trial 17.
 (b) Stress vs displacement graph for trial 17.

8.3.2 Observations:

The optical micrographs below correspond to the points in the graph for trial 17.

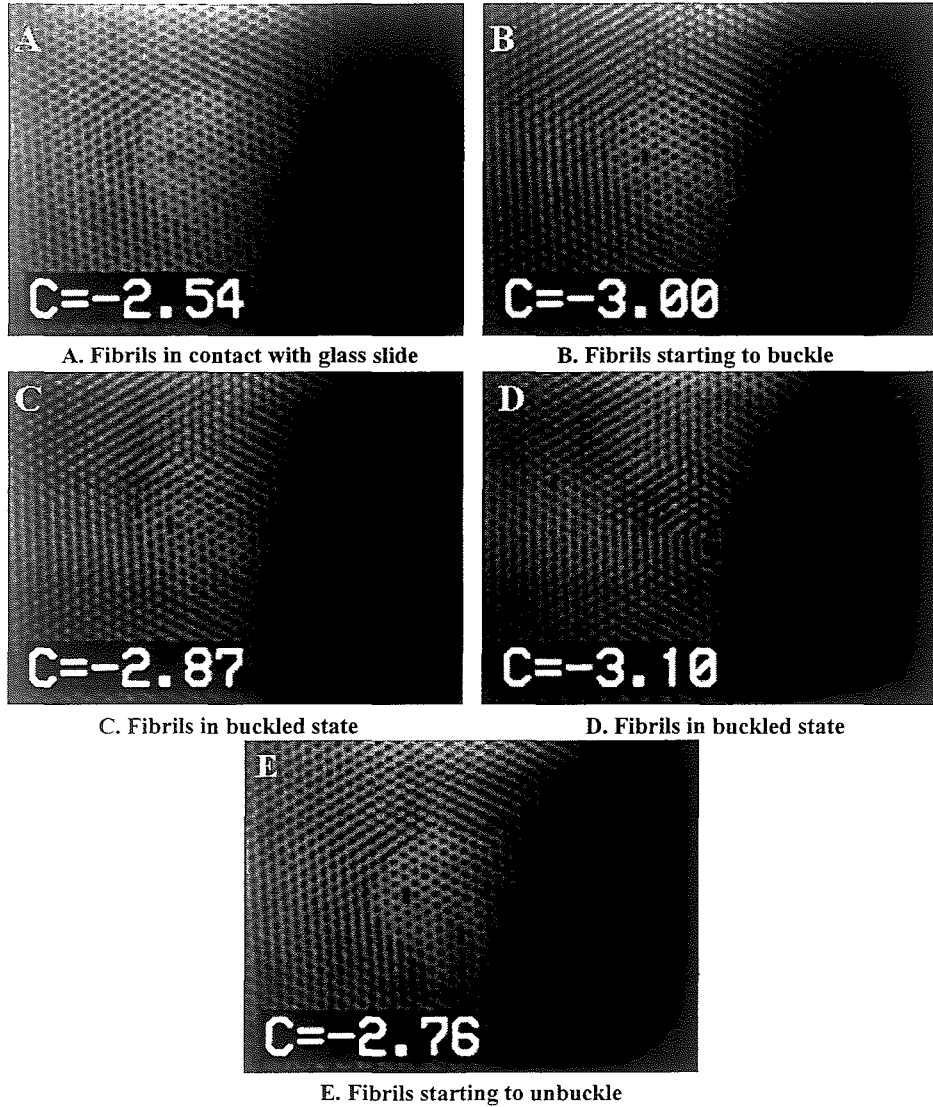


Fig 8.3.2: Visual indications of buckling and unbuckling for sample

8.3.3 Observations

A represents the situation where load is not applied to the sample and the graph that is parallel to the x-axis. The indenter moves downward, but it hasn't come into contact with the sample. The compressive stress increases with increase in displacement of the indenter up to point B. Here the cross-sections of the fibrils lose contact with the glass slide and the fibrils start to buckle. This point is recorded as the critical buckling stress for the sample.

The graph between B and C is almost parallel to the y-axis as seen in sample 1. The decrease in stress with buckling seems the sharpest in the samples where fibrils have minimum spacing. The buckling starts at B and with the slight decrease in stress the fibrils buckle completely at C. After this point, the fibrils remain in buckled form till point D. The fibrils also appear to buckle in a circular pattern. The graph continues this trend until the indenter rises at D. Now the stress decreases with upward displacement.

At point E, the fibrils appear to have unbuckled. The cross-sections of the fibrils come into contact with the glass slide and appear dark again. In this sample, during unbuckling, the stress doesn't seem to increase with the displacement as seen with

EXPERIMENTAL OBSERVATIONS AND MEASUREMENTS

previous samples with thicker fibrils. However, the slope of stress v/s displacement decreased with unbuckling.

Stress at buckling: 20030.2 N/m²

Stress at unbuckling: 10329 N/m²

8.4 Structure 5: 16 micron side x 53 micron height (medium spacing)

The approximate area of the sample used for experiments is 13mm x 13mm.

8.4.1 Raw data and Stress-Displacement plots

Trial 2:

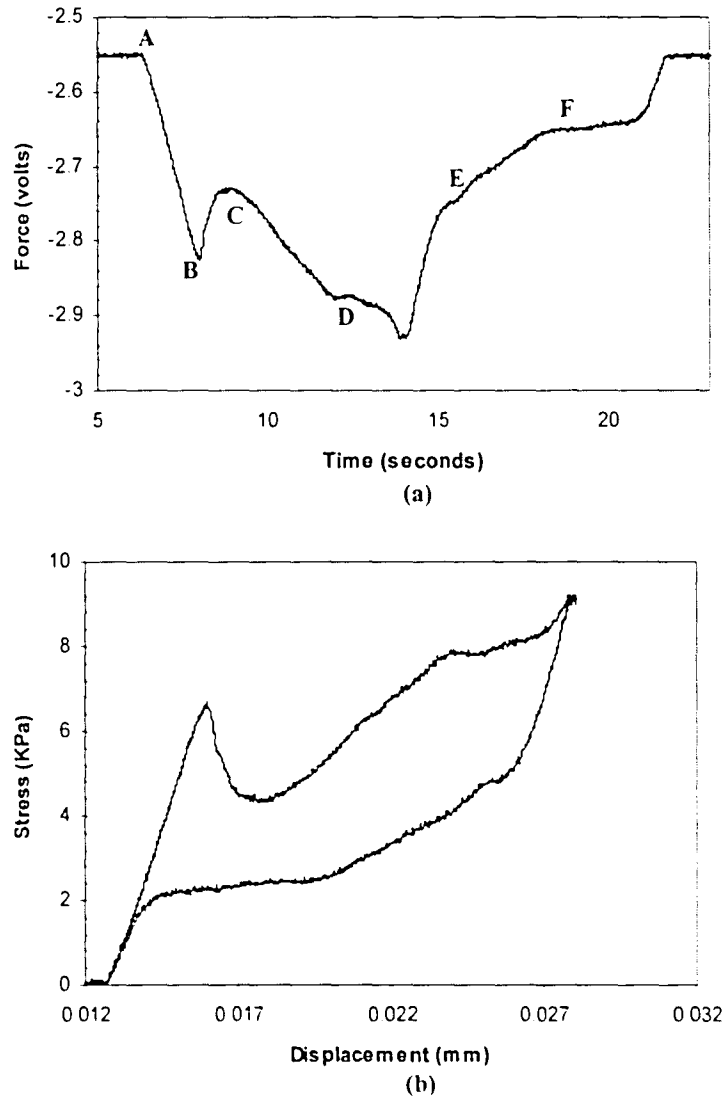
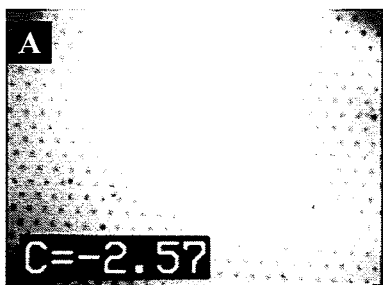


Fig 8.4.1: (a) Raw data representing force vs time graph for the sample during trial 2. (b) Stress vs displacement graph for trial 2.

8.4.2 Optical Micrographs:

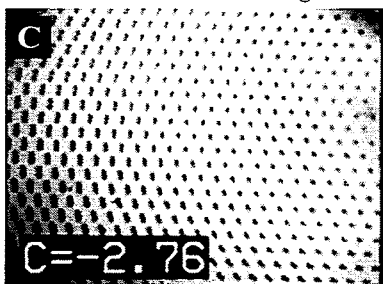
The optical micrographs below correspond to the points in the graph for trial 2.



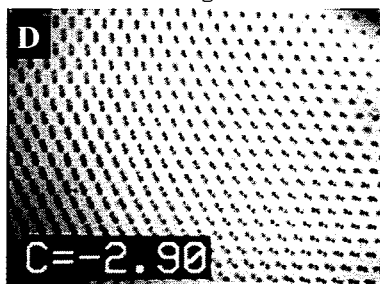
A. Fibrils in contact with glass slide



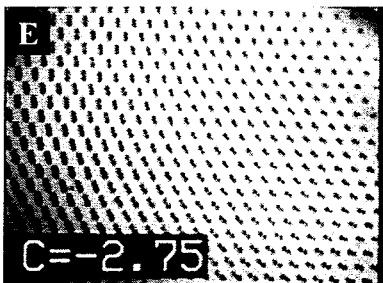
B. Fibrils starting to buckle



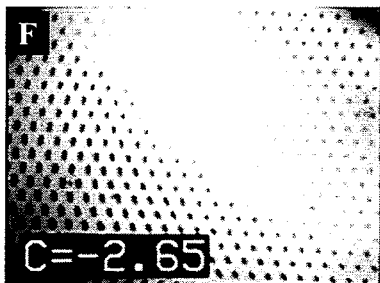
C. Fibrils in buckled state



D. Fibrils in buckled state



E. Fibrils starting to unbuckle



F. Fibrils in unbuckled state

Figures 8.4.2 (A-F): Visual indications of buckling and unbuckling for the sample

8.4.3 Observations

A represents the situation where load is not applied to the sample and the graph that is parallel to the x-axis. The indenter moves downward, but it hasn't come into contact with the sample. The compressive stress increases with increase in displacement of the indenter unto point B. Here the cross-sections of the fibrils lose contact with the glass slide and the fibrils start to buckle. This point is recorded as the critical buckling stress for the sample.

The buckling between B and C is a little less abrupt than seen in samples with lesser spacing between the fibrils. The buckling starts at B and with the slight decrease in stress the fibrils buckle completely at C. After this point, the fibrils remain in buckled form through point D. Between D and E, the slope of the graph changes reflecting the rotation of the fibrils. The compression in the sample continues until E. At E, the indenter rises and the stress decreases with upward displacement.

At point F, the fibrils start to unbuckle. At G, The cross-sections of the fibrils come into contact with the glass slide and appear dark again. The fibrils have completely unbuckled.

EXPERIMENTAL OBSERVATIONS AND MEASUREMENTS

Stress at buckling: 6611.11 N/m²

Stress at unbuckling: 2172.25 N/m²

8.5 Structure 6: 16 micron side x 53 micron height (large spacing)

The approximate area of the sample used for experiments is 13mm x 13mm.

8.5.1 Raw data and Stress-Displacement plots

Trial 4:

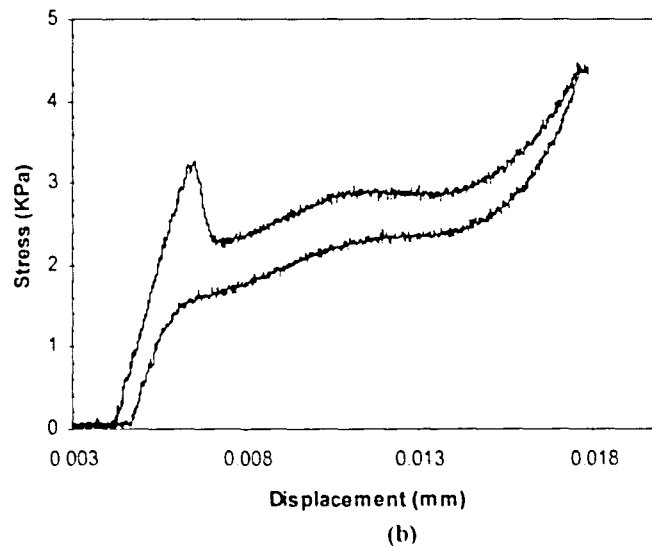
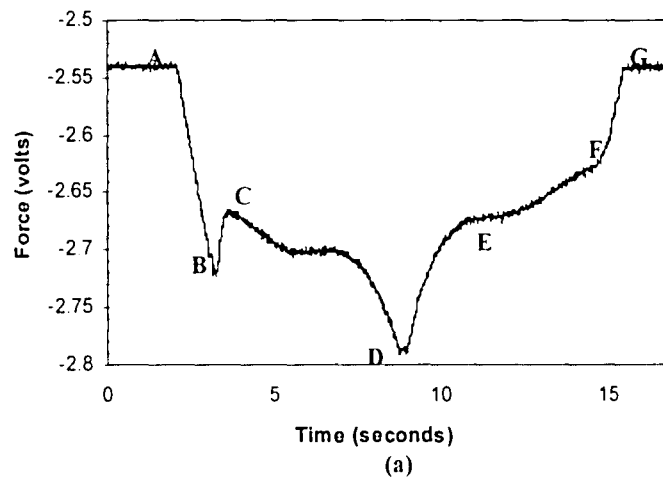
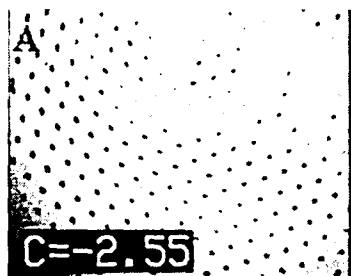


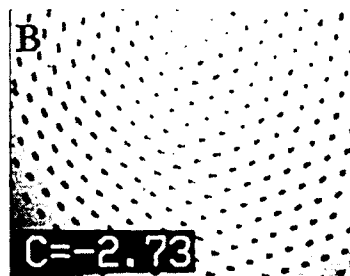
Fig 8.5.1: (a) Raw data representing force vs time graph for the sample during trial 4. (b) Stress vs displacement graph for trial 4.

8.5.2 Optical Micrographs:

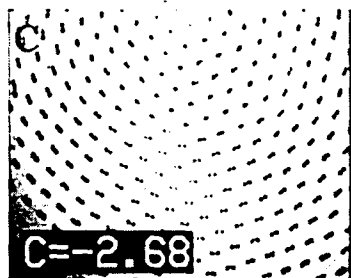
The optical micrographs below correspond to the points in the graph for trial 4.



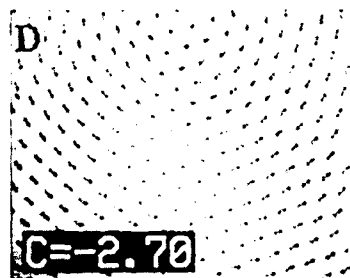
A. Fibrils in contact with



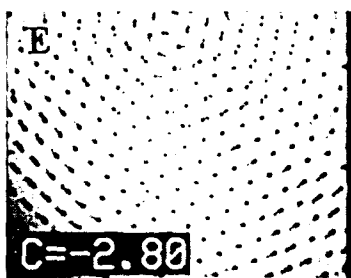
B. Fibrils starting to buckle



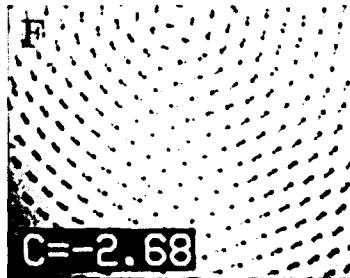
C. Fibrils in buckled state



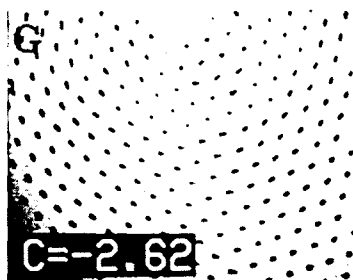
D. Fibrils in buckled state



E. Fibrils in buckled state



F. Fibrils starting to unbuckle



G. Fibrils in unbuckled state

Figures 8.5.2 (A-G): Visual indications of buckling and unbuckling for the sample

8.5.3 Observations

A represents the situation where load is not applied to the sample and the graph that is parallel to the x-axis. The indenter moves downward, but it hasn't come into contact with the sample.

The compressive stress increases with increase in displacement of the indenter unto point B. Here the cross-sections of the fibrils lose contact with the glass slide and the fibrils start to buckle. Also, the fibrils appear to buckle in a circular pattern. This point is recorded as the critical buckling stress for the sample.

The buckling between B and C takes place a little less abrupt than seen in samples with less spacing between the fibrils. The fibrils buckle completely at C. After this point, the fibrils remain in buckled form through point D. Between D and E, the slope of the graph changes reflecting the rotation of the fibrils around their own axes. The compression in the sample continues until E. At E, the indenter rises and the stress decreases with upward displacement.

EXPERIMENTAL OBSERVATIONS AND MEASUREMENTS

At point F, the fibrils start to unbuckle. At G, The cross-sections of the fibrils come into contact with the glass slide and appear dark again. The fibrils have completely unbuckled.

Stress at buckling: 3235.5 N/m^2

Stress at unbuckling: 1477.5 N/m^2

Chapter 9.

BUCKLING THEORY

9.1 Discussion

Leonhard Euler showed that there was a critical load for buckling of a slender column. A column is a common case of a compression member. With any smaller load, the column would remain straight and support it. With any larger load, the least disturbance would cause the column to bend sideways with an indefinitely large displacement; that is, it would buckle [14-16].

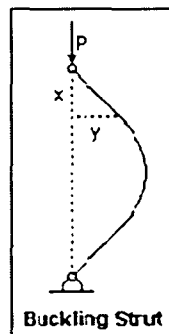


Figure 9.1: Schematic figure of a typical buckling strut

The simplest case is that of a column pinned at both ends, that is, free to rotate, under a load P .

Let x be the distance along the column, and y its displacement to the side. The bending moment at any point x is P_y . The bending moment is related to the curvature by

$$P_y = M = -EI \frac{d^2 y}{dx^2} \quad \text{-eqn 9.1}$$

since for small y the second derivative is the reciprocal of the radius of curvature.

E is Young's modulus, and I is the moment of inertia of area of the cross-section of the column.

The differential equation is solved with the result:

$$y = A \sin ax + B \cos ax \quad \text{where} \quad a^2 = \frac{P}{EI} \quad \text{-eqn 9.2}$$

$$B = 0, \text{ since } y(0) = 0$$

The condition $A \sin aL = 0$ must also be satisfied, where L is the length of the column.

This means that $aL = \pi, 2\pi, \dots$, or the smallest value of P is given by

$$P' = \frac{\pi^2 EI}{L^2} \quad \text{-eqn 9.3}$$

The constant A itself remains indeterminate.

The interpretation of this result is that for $P < P'$ the column remains straight and $A = 0$.

For $P > P'$, the column is unstable and buckles. P' is the critical load for buckling.

A column *pinned* at both the ends is free to rotate under a load P. If the ends of the column are *clamped*, that is, prevented from rotating, the buckling curve changes from a half-wavelength sine to a full-wavelength cosine, effectively halving the length of the column, and increasing the critical load by a factor of 4.

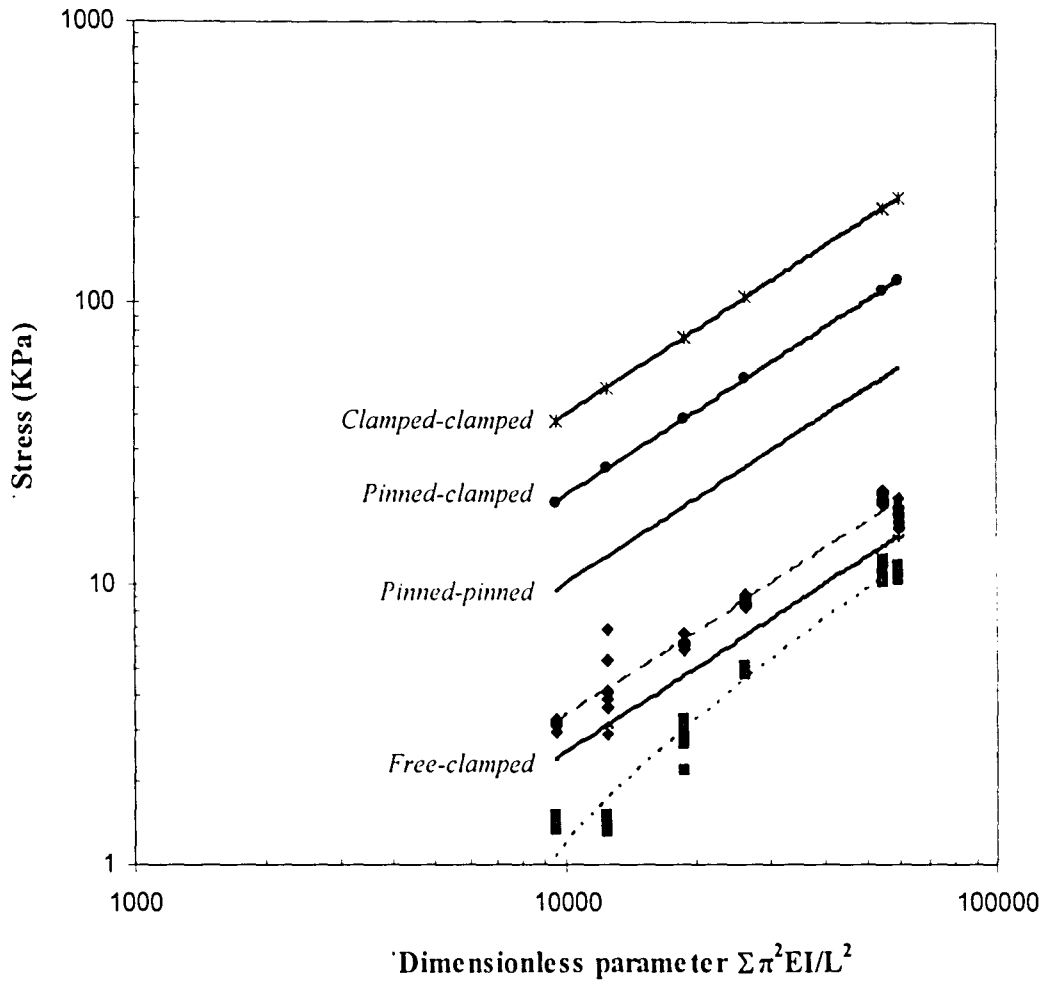
Some classical boundary conditions of columns are *pinned-pinned*, *free-clamped*, *clamped-clamped*, and *pinned-clamped*. The equations represent stress in N/m².

Boundary condition	Equation
<i>pinned-pinned</i>	$y = x$
<i>free-clamped</i>	$y = 0.25x$
<i>clamped-clamped</i>	$y = 4x$
<i>pinned-clamped</i>	$y = 2.05x$

Table 9.1: The equations of lines on the graph of stress (in Pa) vs the dimensionless parameter $\pi^2 EI/L^2$ representing the classical boundary conditions for a buckling strut

The above conditions are plotted on a graph of stress (in Pa) vs the dimensionless parameter $\pi^2 EI/L^2$. The buckling stresses and unbuckling stresses observed with the samples are plotted along with the above conditions.

9.2 Plots of Buckling theory and Experimental values



◆ Buckling stresses: slope = 0.33 ■ Unbuckling stresses: slope = 0.21

Fig 9.2: Log-log plot of stress (in KPa) v/s the dimensionless parameter $\pi^2 EI/L^2$

The buckling and unbuckling loads are recorded for the various samples tested.

The corresponding stresses are calculated and plotted in the above graph.

9.3 Observations

The critical stresses (in Pa) for the tested samples are observed to follow the equations given:

Stresses at Buckling: $y = 0.33x + 63.25$

Stresses at Unbuckling: $y = 0.21x - 933.04$

The values of the buckling as well as unbuckling stresses vary with the spacing between the fibrils. Among the samples tested, the ones with largest spacing (i.e. about 3 times the critical spacing calculated) appear to have the lowest values of critical stress. The samples with medium spacing (i.e. about twice the critical spacing calculated) appear to have greater values of load required and the samples with the smallest spacing have the greatest values of buckling and unbuckling load.

Values of critical stresses for samples with medium spacing ≈ 2 times the critical stresses for the sample with largest spacing.

Values of critical stresses for samples with small spacing ≈ 6.5 times the critical stresses for the sample with largest spacing.

Chapter 10.

CONCLUSIONS

Well-defined fibrillar structures are designed and fabricated using microlithographic patterning techniques. Indentation experiments are performed on the structures to study the phenomenon of buckling and unbuckling. The differences previously observed between buckling and unbuckling forces are explored further. The experimental setup is also used to measure the modulus of PDMS used for stress calculations.

The buckling and unbuckling loads are recorded from the indentation experiments performed on the various samples tested. These observed buckling and unbuckling load values are used to calculate the corresponding stress values which are compared with those of struts with classical boundary conditions.

The critical stresses during buckling are observed to follow $y = 0.33x + 63.25$ (with a standard deviation of 0.01) while those at unbuckling seem to follow $y = 0.21x - 933.04$ (with a standard deviation of 0.003). During buckling, the fibrils seem to move more freely as compared to while they unbuckle.

The values of critical stresses at buckling or unbuckling for samples with medium spacing (i.e. almost equal to twice the critical spacing) are approximately 2 times the stress for the sample with largest spacing. The samples with the smallest spacing (i.e. almost equal to critical spacing) appear to require approximately 6.5 times the critical stress as compared to the samples with the largest spacing. The stresses developed in the samples, however, seem independent of the rate of loading.

REFERENCES

1. Kellar Autumn, Yiching A. Liang, S. Tonia Hsieh, Wolfgang Zesch, Wai Pan Chan, Thomas W. Kenny, Ronald Fearing, Robert J. Full, "Adhesive force of a single gecko foot-hair", *Nature*, 2000 405 681-685.
2. E. Arzt, S. Gorb, R. Spolenak, "From micro to nano contacts in biological attachment devices", *Proceedings of the National Academy of Sciences*, 100 (19) 10603-10606 (2003).
3. Duncan J. Rischick, Christopher C. Austin, Ken Petren, Robert N. Fisher, Jonathan B. Losos, Olaf Ellers, "A comparative analysis of clinging ability among pad-bearing lizards," *Biological Journal of the Linnean Society* (1996) 59 21-35.
4. Kellar Autumn, Metin Sitti, Yiching A. Liang, Anne M. Peattie, Wendy R. Hansen, Simon Sponberg, Thomas W. Kenny, Ronald Fearing, Jacob N. Israelachvili, Robert J. Full, "Evidence for van der Waals adhesion in gecko setae", *Proceedings of the National Academy of Sciences* (2002) 99 19, 12252-12256.
5. Matthias Scherge, Stanislav N. Gorb, *Biological Micro and Nanotribology: Nature's Solutions*, Springer-Verlag (Berlin) 2001.
6. S.N. Gorb, *Proc. R. Soc. London B* 265 747-752 (1998).
7. Anand Jagota, Stephen J. Bennison, "Mechanics of Adhesion Through a Fibrillar Microstructure," *Integrative and Comparative Biology*, 42 1140-1145 (2002)

-
-
8. N.J. Glassmaker, A. Jagota, C-Y. Hui, J. Kim, "Design of Biomimetic Fibrillar Interfaces: 1. Making Contact," *Journal of the Royal Society: Interface* 1 [1] 22-33 (2004).
 9. C-Y. Hui, N.J. Glassmaker, T. Tang, A. Jagota, "Design of Biomimetic Fibrillar Interfaces: 2. Mechanics of Enhanced Adhesion," *Journal of the Royal Society: Interface* 1 [1] 35-48 (2004).
 10. C.Y. Hui, A. Jagota, Y.Y. Lin, E.J. Kramer, "Constraints on Micro-Contact Printing Imposed by Stamp Deformation," *Langmuir* (2002)18 1394-1404
 11. Kenneth G. Sharp, Gregory S. Blackman, Nicholas J. Glassmaker, Anand Jagota, C-Y. Hui, "The Effect of Stamp Deformation on the Quality of Microcontact Printing: Theory and Experiment," *Langmuir* (2004) 20, 6430-6438.
 12. Johnson, K.L, Kendall, K., and Roberts, A.D., Surface Energy and the contact of elastic solids, *Proceeding of Royal Society* (1971) A324, 301.
 13. Geim, A. K., Dubonos, S. V., Grigorieva, I. V., Novoselov, K. S., Zhukov, A. A. & Shapoval, S. Y. 2003 Microfabricated adhesive mimicking gecko foot-hair. *Nature Materials* 2, 461–463.
 14. Crandall, S. H., Dahl, N. C. & Lardner, T. J. 1978, *An Introduction to the Mechanics of Solids*. Kogakusha: McGraw- Hill.
 15. Timoshenko, S. P. & Gere, J. M. 1961, *Theory of elastic stability*. New York: McGraw-Hill.
 16. Johnson, K. L. 1985, *Contact mechanics*. Cambridge: Cambridge University Press.

VITA

Name Ajita Rajan
Date of Birth May 24, 1982
Place of Birth Mumbai, India
Parents Dr. M.G.Ramakrishna. Rajan & Dr. (Mrs.) Rema Rajan

INSTITUTIONS ATTENDED

Secondary Atomic Energy Junior College, Mumbai
Graduation: March, 1999
Collegiate Bachelor of Engineering (Chemical Engineering)
University of Mumbai (Bombay)
Graduation: Fall, 2003
Graduate Completed the Requirements for the Master of Science degree in
Chemical Engineering
Lehigh University
For graduation in January, 2006.

PROFESSIONAL EXPERIENCE

Internship at A & A bio-ware: Reagents for Immunoassay Laboratories, 2002
Purification of antiserum by ammonium sulfate precipitation and gel filtration column chromatography as pre-preparation for incorporating into immunoassay reagents.

Research Project (Undergraduate final year 2002-03):
Bhabha Atomic Research Center, Mumbai, India
Membrane Separation Processes focusing on Reverse Osmosis

TEACHING ASSISTANT

CHE 461 (ME 442/ENGR 452): Mathematical Methods in Engineering
Linear vector spaces; eigenvalues, eigenvectors, and eigenfunctions; First and higher-order linear differential equations with initial and boundary conditions; Sturm-Liouville problems; Green's functions. Special functions; Bessel, etc.; Qualitative and quantitative methods for nonlinear ordinary differential equations; phase plane; Solutions of classical partial differential equations from the physical sciences; transform techniques; method of characteristics.

**END OF
TITLE**